UNIVERSITY OF TWENTE

MSc THESIS BIOMEDICAL ENGINEERING

Axial superresolution using nanophotonic manipulation: How accurate can we be?

Author:
Robert van DINTEREN

Supervisors:
Dr. Christian BLUM
Ing. Robert MOLENAAR
Prof. Mireille CLAESSENS
Dr. Cees OTTO

A thesis submitted in fulfillment of the requirements for the degree of MSc of Biomedical Engineering

NBP - Nanobiophysics

September 3, 2020

"Imagination will often carry us to worlds that never were. But without it we go nowhere."

- Carl Sagan (Cosmos, Ch. 1)

UNIVERSITY OF TWENTE

Abstract

Faculty of Science and Technology
MIRA Institute for Biotechnology and Technical Medicine

MSc of Biomedical Engineering

Axial superresolution using nanophotonic manipulation: How accurate can we be?

by Robert van DINTEREN

The nanoscale topography of the cell membrane is often overlooked. However, the deformation of the cell membrane plays a role in many processes. Current imaging methods struggle to measure nanoscale features on live cells. A novel approach has been developed using photonic emitter manipulation to achieve axial sub-20 nm resolution without directly interacting with the surface. Here we continue characterizing this approach. We observe that the feedback-mechanism can be influenced by the surface, hindering reproducibility. We calculate the axial resolution from experiment and simulation, displaying its distance-dependency and the working range of the technique. We show an undesirable change to the point spread function under effect of the emitter manipulation. The technique shows promise for axial superresolution imaging. However, there are fundamental obstacles that must be overcome in order to measure on live cells.

Acknowledgements

This thesis has been long in the works and I owe a huge debt of gratitude to all the people involved. My thanks firstly to the members of the Nanobiophysics group. Christian, for offering direction when I was lost and sticking it out with me until the very end. Robert, for his endless support in the optics lab and for fixing things that had to be broken. I very much enjoyed our weekly meetings where there was space for input of any kind.

I would like to take this opportunity to also thank Mireille. For her scientific vigor that unfolded on me during her inaugural address, her incessant kindness, and helping me land the internship in Munich that otherwise would never be.

I would have gotten nowhere without the assistance of Yvonne and Kirsten, who were always eager to help me find the way in the chemical lab. My thanks go out to Amin, for showing me how to create lipid vesicles in the lab, and Jacco for optimizing their deposition. To Carla Annink, with who I fervently took on the task of homogeneously covering gratings with lipids. The cleaning of glassware will stay with me forever. To Sylvia for being her radiant self, and giving me those little nudges when I needed them most.

I would like to thank Wesley, Matthijs, Maik and Carlo. For either proof-reading my thesis, or giving advice on topics that were just out of my reach.

Finally, I would like to thank my parents, to whom this thesis is dedicated.

Contents

List of Figures

List of Tables

List of Abbreviations

AFM	**A**tomic **F**orce **M**icroscopy
AOTF	**A**cousto-**O**ptical **T**unable **F**ilter
APD	**A**valanche **P**hoto-**D**iode
BP	**B**and **P**ass filter
FWHM	**F**ull **W**idth **H**alf **M**aximum
LB	**L**angmuir-**B**lodgett
LD	**L**aser **D**iode
LDOS	**L**ocal **D**ensity of **O**ptical **S**tates
LED	**L**ight **E**mitting **D**iode
LP	**L**ong **P**ass filter
NA	**N**umerical **A**perture
ND	Neutral Filter
PS	**P**oly**s**tyrene
PSD	**P**osition **S**ensistive **D**etector
PSF	**P**oint **S**pread **F**unction
RhB	**Rh**odamine **B**
Rh101	**Rh**odamine **101**
SP	**S**hort **P**ass filter
TCSPC	**T**ime-**C**orrelated **S**ingle **P**hoton **C**ounting
UV	**U**ltra**v**iolet

To my parents

Chapter 1

Introduction

The machinery of the human cell is marvelous. Every second our DNA is copied, translated, and interpreted at an incredible rate to form the very building blocks of life. Directional intracellular transport is performed on biological equivalent of train rails by motor proteins [1]. The cell membrane acts as a barrier that is so extremely thin, but still allows for controlled transport, sensing and can grow or change shape as needed [2].

Often undesirable, the blunders of these cellular processes are however what allow for the rise of change. The fact that mutations in our DNA allows for the evolution of species already reveals the strong connection between what happens at the nanoscale and the larger world. Understanding the workings of the cell is essential to tackle many diseases that are still prevalent today. Uncontrollable cell growth, cancer, is caused by mutations in DNA. Protein aggregation is believed to play a central role in Parkinson's disease [3]. But also, interactions of proteins with certain membranes should be understood to uncover functional or pathological mechanisms. In this study, we are particularly interested in measuring the topography of the cell membrane.

1.1 The Cell Membrane

It is often necessary that the products and mechanisms within a cell are isolated from their environment in a controlled way. The cell membrane fulfills this role perfectly. Simple bacteria only have a single cell membrane. Our cells, however, also contain internal membranes that enclose intracellular compartments that form organelles. All these membranes function as a high selective barrier, and subtle differences in their composition give each organelle its distinctive character.

The lipid bilayer has been firmly established as the basis for cell membranes. The lipids in these membranes are amphiphatic; each lipid has a hydrophilic ("water-loving") head and a hydrophobic ("water-fearing") tail. This property drives the lipids to self-assemble into bilayers in an aqueous environment as the lipid tails bundle together. The lipid bilayer is however not the only constituent of the cell membrane, transmembrane and peripheral membrane proteins are also associated with the membrane, either directly or through some kind of anchoring system (Fig. 1.1) [2, 5].

In addition to its barrier function, the lipid bilayer provides the potential for budding, tubulation, fission and fusion, which are essential for cell division and intracellular membrane trafficking [5].

The fluidity and in part the shape of a membrane depends on its composition. The composition can change by a difference in hydrocarbon tails. The "shape" of a lipid molecule depends on the relative spatial hindrance of its head and tail. As such, cone-shaped lipids can cause curvature. Mixtures of different lipids can lead

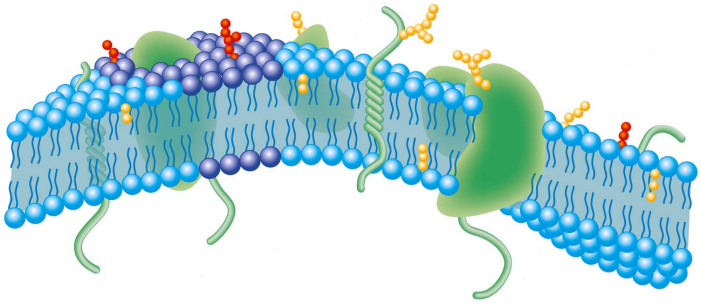

FIGURE 1.1: **The structure of a cell membrane.** The lipid bilayer forms the basis of the cell membrane. Proteins, glycolipids and lipid rafts add additional functionality. Adapted from *"Our evolving view of plasma membrane domains"* [4].

to totally difference structural arrangements in the end (Fig. 1.2) [6]. The addition of sterols, such as cholesterol, can also aid in membrane curvature. Specific properties of these phases determine the orientation and mobility of the membrane lipids and proteins, and thus affect the membrane functionality [5].

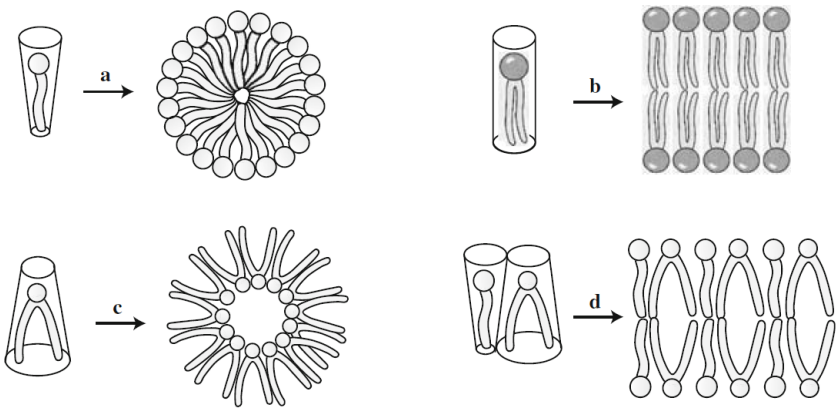

FIGURE 1.2: The relationship between the structural shape of a lipid molecule and the way it self-assembles in an aqueous environment [6].

More extreme deformations can occur due to protein involvement. For example, the cell membrane of many cell types are covered with clathrin coated pits that allow for receptor-mediated endocytosis [7], and actin dynamics alter the topography, creating structures such as lamellipodia and filopodia [8]. Caveolae are bulb-shaped invaginations of the plasma membrane of roughly 50-80 nm in diameter that function in a multitude of cellular processes [9]. They respond to mechanical stress, under which they disassemble, and regulate cellular signaling [10, 11].

It becomes clear that the deformation of the cell membrane is a frequent phenomenon that plays a role in many processes. Furthermore, many of the aforementioned changes operate on a nanometer scale, which causes a challenge for the imaging of these structures.

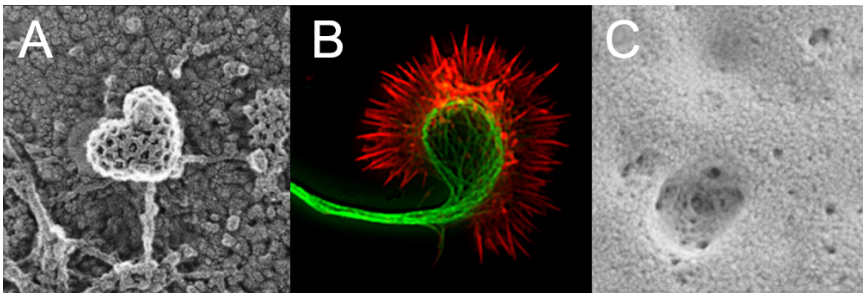

FIGURE 1.3: **Images of cell membrane deformations.** A) SEM image of a clathrin coated pit [12] B) Fluorescence image of a cortical axon, actin filaments (red) occupy the lamellipodium, microtubules (green) occupy the axon and central region of the growth cone [13] C) SEM image of caveloae [14].

1.2 Imaging Membrane Topography at the Nanoscale

The topography of the cell membrane is often ignored when interpreting microscopy data. Even acknowledging the global curvature disregards the fact that there are ridges, undulation and projections on the surface of live cells [15]. These changes in membrane organization are not apparent when using fluorescence microscopy and higher resolution techniques are required to visualize these features in membrane topography.

1.2.1 Optical Super-Resolution

It was late in the 19th century when Ernst Abbe recognized that the resolution of light microscopy would be limited to roughly half the wavelength of light. Fortunately, microscopy has increased its resolving power over the last decades. The spatial resolution of a confocal microscope is already slightly better than it's wide-field counterpart and brings a dramatic improvement in effective axial resolution compared to more conventional techniques [16].

$$d_{xy,\,confocal} \approx \frac{0.4 \cdot \lambda}{NA}$$
$$d_{z,\,confocal} \approx \frac{1.4 \cdot n\lambda}{NA^2}$$

Where λ is the wavelength, NA the numerical aperture and n the refractive index.

Super-resolution approaches such as Stimulated Emission Depletion (STED) Microscopy and Structured Illumination Microscopy (SIM) use patterned illumination to spatially modulate the fluorescence behavior of molecules, so that within a diffraction limited region, not all of them emit simultaneously [17]. The technique uses high intensity light in order to reduce the size of the effective fluorescent spot. Caution must therefor therefore taken not to damage the sample.

Other prevalent super-resolution techniques that have proven to beat - or cheat - the diffraction limit are Stochastic Optical Reconstruction Microscopy (STORM) and Photo-Activated Localization Microscopy (PALM) [18]. These approaches take advantages of single-molecule imaging by sparse activation within the diffraction-limited region, after which a high-resolution image is then reconstructed.

1.2.2 Electron Microscopy

The transmission electron microscope (TEM) is similar to a light microscope but uses a beam of electrons instead of a beam of light. It was invented in the early 1930s, but there were some challenges involved when imaging biological samples. Such samples are hydrated, radiation sensitive, exhibit poor contrast and are often too thick to be imaged intact [19]. To overcome these challenges, methods were developed to chemically fix and stain the samples, embed them in plastic resin and section them with a microtome [2]. During these sample preparations however, the cell is killed.

1.2.3 Scanning Probe Microscopy

There are several scanning probes that are used to image nanoscale topography. The well-known atomic force microscope (AFM) uses the interaction between the cantilever's tip and the sample to determine topography (Fig. 1.4). Making contact with the soft membrane however induces surface deformation [20], using this technique therefor leads to the visualization of the cytoskeleton rather than the shape of the cell membrane [21].

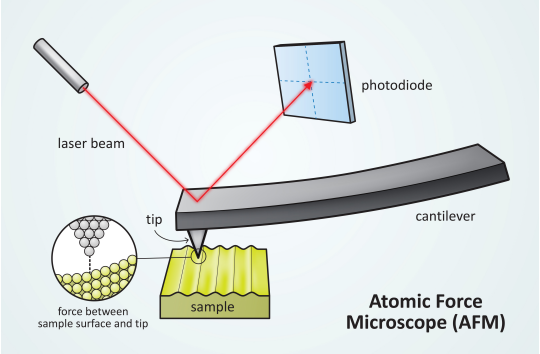

FIGURE 1.4: **A schematic representation of an AFM system.** The change in cantilever deflection will result in a different voltage measurement by the quadrant detector [22].

A scanning method that is contact-free is scanning ion conductance microscopy (SICM). It uses the change in electrical resistance to detect the distance between the scanning tip and the insulator [21]. Even though the technique is essentially contact free, the optimal tip-sample distance is equal to half of the tip diameter [23]. This means that the tip has to be only at a few nm from the cell, which can interact with steep protrusions or molecules that are sticking out of the membrane.

1.2.4 Metal Induced Energy Transfer

The last nanoscopy technique that will be discussed is the Metal Induced Energy Transfer (MIET). This technique is similar to Förster Resonance Energy Transfer (FRET), which is based on electromagnetic-field-mediated energy transfer from an optically excited donor to an acceptor allowing to measure distances on the nanometer scale using fluorescence imaging. In MIET however, instead of two fluorophores interacting with each other, the acceptor is replaced by a thin metallic film which increased the distance range by an order of magnitude. The energy transfer between the donor fluorophore and the metallic film allows for the localization of fluorescent molecules over a distance of more than 100 nm [24]. Unfortunately the sample of interest is always imaged directly on the flat metallic surface.

1.3 Outlook of the Thesis

The initial study of our group was focused on the emission rates and quantum efficiencies of fluorescent proteins by modifying their emission rates under influence of a mirror at fixed distances [25]. Following this study, a photonic emitter manipulation probe was designed to have precise control over the mirror position [26]. The probe consists of a spherical gold mirror that is controlled by a closed-loop feedback of an AFM cantilever. This probe was consequently used to measure the dark fraction of fluorescent proteins [27]. The same technique was later used for initial topography measurements at the nanoscale [28].

The work presented in this thesis continues with further topography measurements and characterizes the reproducibility, obtainable axial resolution and other probe effects.

In Chapter 2, we explain the workings of the photonic emitter manipulation probe. In Chapter 3, the working set-up and the manipulation probe are explained together with several techniques that were used to fabricate samples. Chapter 4 to 7 report on the experiments that were performed during this study. In Chapter 4, we investigate the reproducibility of the lifetime manipulation. In Chapter 5, we define and determine the obtainable resolution of the technique. In Chapter 6, we look at the influence of the probe on the lateral resolution and inspect what we can practically resolve. In Chapter 7, a method to improve the working range is suggested and further limits are explored. Finally, in Chapter 8, we draw conclusions of the realized work and propose improvements and recommendations for upcoming research.

Chapter 2

Background

In this chapter we introduce the theoretical background of the project. First, we explain the workings of fluorescence and define the lifetime of a fluorophore. Second, we give a principal explanation on how the fluorescence lifetime can be manipulated using a metallic mirror.

2.1 Fluorescence

The use of fluorescence is indispensable in microbiology. Fluorescence imaging allows for the localization and measurements of intracellular molecules, down to the single molecule level [29]. Fluorescence is one of two categories of luminescence and occurs when an excited electron returns to the ground state and rapidly emits a photon.

An essential diagram when talking about fluorescence is the Jablonski diagram (Fig. 2.1). Here the ground, first and second electronic state are shown by S_0, S_1 and S_2 respectively. Each electronic state also contains numerous smaller vibrational energy levels, which are depicted by 0, 1, 2, etc.

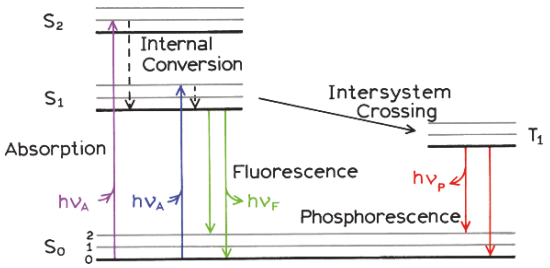

FIGURE 2.1: **A Jablonski diagram.** In this diagram the states are arranged vertically by energy. The vibrational grounds states of each electronic state (S_x) are indicated with thick lines [29].

After a fluorophore absorbs a photon, several processes usually occur. Due to the absorption, the fluorophore is excited to some higher vibrational level of S_1 or S_2. Immediately after, the fluorophore rapidly relaxes to the lowest vibrational level. This internal conversion occurs within 10^{-12} s or less. This is much faster than the typical lifetimes of fluorescent molecules, approximately 10^{-8} s. Therefore fluorescent emission generally results from the lowest energy vibrational state of S_1. The emission to the ground state can also occur to higher vibrational levels as is indicated by the green arrows in the Jablonski diagram (Fig. 2.1).

An interesting consequence of the absorption and emission to higher vibrational levels is that these phenomena occur in a set energy range. Therefore, fluorophores

have a typical absorption and emission spectrum. An example of such spectra is visible for Rhodamine 101 (Fig. 2.2). Another consequence is that the emitted photons generally have a lower energy and therefore a longer wavelength than the absorbed photon. The energy difference lost is partly due to the vibrational transitions.

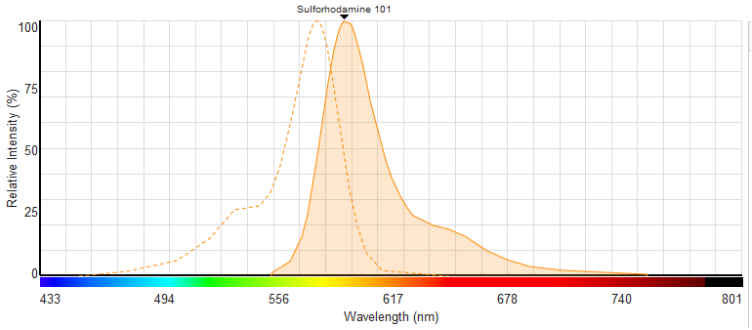

FIGURE 2.2: **The absorption and emission spectrum of Rhodamine 101.** The fluorophore is excited at a relatively high energy (short wavelength), after which it can emit a fluorophore with a lower energy (longer wavelength) due to energy losses [30].

2.1.1 Fluorescence Lifetime

Two of the most important characteristics of a fluorophore are the fluorescence lifetime and quantum yield. The quantum yield is the fraction of fluorophores that decay through emission, and is given by

$$q = \frac{\Gamma_R}{\Gamma_R + \Gamma_{NR}}$$

Where Γ_R is the rate of radiative decay, and Γ_{NR} is the rate of non-radiative decay. The lifetime of a fluorophore is defined by the average time the molecule spends in the excited state prior to returning to the ground state, and is given by

$$\tau = \frac{1}{\Gamma_R + \Gamma_{NR}}$$

2.1.2 Time Correlated Single Photon Counting

Fluorescent emission is a random process. That is why the definition of lifetime is simply the *average* value of the time spent in the excited state. The initial population of fluorophores in an excited state (n_0) decays with a rate $\Gamma_R + \Gamma_{NR}$ according to

$$\frac{dn(t)}{dt} = (\Gamma_R + \Gamma_{NR})n(t)$$

This results in an exponential decay of the excited state population.

$$n(t) = n_0 exp(-t/\tau)$$

The fluorescence lifetime can be determined by fitting the data to certain decay models. In Time-Correlated Single-Photon Counting (TCSPC) this is exactly what happens. The sample is excited with a pulse of light and the time between this pulse and the observed emitted photon is stored in a histogram (Fig. 2.3). It is important to only detect a single photon per excitation pulse to keep the data statistically pure

to prevent histogram bias towards shorter lifetimes, since only the first photon will be observed. Therefore, conditions are adjusted to perform TCSPC and typically only 1 photon per 100 excitation pulses is detected.

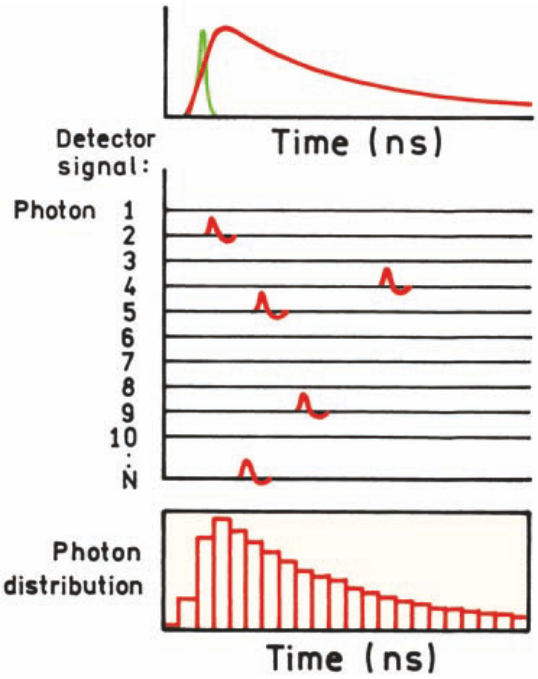

FIGURE 2.3: **Time-Correlated Single-Photon Counting.** Emitted photons are detected and added to create a photon distribution. Fitting the distribution can determine the fluorescence lifetime. [29]

2.2 Local Density of States

The spontaneous emission of photons is not a fixed property of the emitter, but also depends on its surroundings. Photons can travel long distances and are very much affected by their environment. Emission close to a flat mirror for example can cause either constructive or destructive interference at the position of the emitter (Fig. 2.4). If the reflected field is in phase, the dipole will be driven harder and it's emission will be enhanced [31]. There is no emission into the waves that destructively interfere, affecting the lifetime depending on the distance from the mirror (due to the change in available modes). This position dependence of the coupling between the emitter and the electromagnetic field is quantified by the number of available modes into which emission can occur, which is roughly speaking the Local Density of States (LDOS).

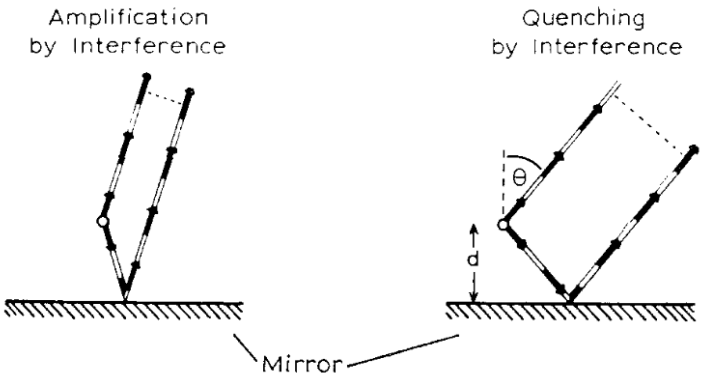

FIGURE 2.4: **Electric dipole radiation interacting with plane mirror [32].** Part of the emitted light is reflected by the mirror and interferes with the non-reflected part. The path difference causes different kinds of interference and can lead to the emitter not radiating in a certain direction at all.

The classical approach considers the emitter to be a forced damped dipole oscillator [31]. Therefore, if the distance between the emitter and mirror is changed, we will observe an oscillation in lifetime. Furthermore, if we increase the distance to the mirror, the oscillation's amplitude decreases. This effects is first shown by Drexhage in 1970, where he showed the lifetime of Eu^{3+} ions to oscillate under the influence of a metallic mirror due to the changes in the LDOS (Fig. 2.5).

An initial study by *Prangsma et al.* [27] at the University of Twente showed that by fitting the measured data to a classical model [33, 34] taking in full account of material properties and environment, the radiative and non-radiative decay rates can be determined. This allowed for the calculation of the bright state quantum efficiency. The oscillating lifetime curve however contains roughly linear section with a clear relation between the lifetime of the emitter and the distance to the mirror. This realization set off further experimental research and design into using this relation to measure surface topography [28].

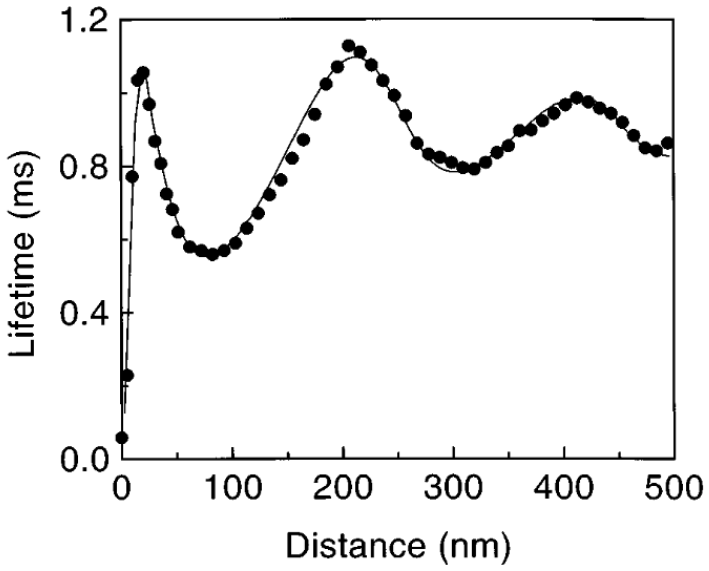

FIGURE 2.5: **Eu^{3+} lifetime as a function of an Ag mirror separation from the ions.** Two regimes are observed: (1) oscillations of the lifetime at "large" distance range and (2) quenching for small distances. The solid line corresponds to the theoretical fit and the circles are the experimental data. This measurement was inspired in the work of Drexhage. [35]

Chapter 3

Materials and Methods

In this chapter we will explain the set-up used in this project. We start by explaining the confocal microscope and the determination of the fluorophore lifetime. Next, we explain how the LDOS probe is fabricated and used to modify the LDOS of the fluorophore. Moreover, the principle of how LDOS manipulation can be used to measure topography is described. Lastly, we explain the alignment and fabrication of samples that are used in this project.

3.1 Experimental Set-Up

The experimental set-up is a combination of a confocal microscope and AFM-controlled LDOS probe. The microscope allows for the determination of fluorophore lifetime through TCSPC analysis, whilst the LDOS probe allows for the tuning of this lifetime.

3.1.1 Confocal Microscope

Lifetime images can be recorded using a custom built, Time-Correlated Single Photon Counting based, confocal microscope (Fig. 3.1).

A supercontinuum white light source (Fianium, SC-400-PP), operating at 20 MHz and generating supercontinuum radiation in the 400 to 2100 nm spectral band, was tuned via an acoustic-optic tunable filter (AOTF) system, which allowed for a tunable excitation wavelength (Crystal Technologies, PC-NI-VIS). The laser light is coupled into a single mode fiber towards the set-up. There, the light is collimated using an objective (4x plan achromat objective, 0.10 NA, Olympus), after which the beam is linearly polarized using a $\lambda/2$ phase plate and a linear polarizer (LPVISB1100-MP). The laser beam was then attenuated using Neutral Filters when necessary.

The incoming beam was filtered by an excitation filter to remove fluorescence and Raman scattering coming from the optical fiber. The glass wedge then directs light towards the objective (C Plan-Apochromat, 63x oil-immersion, 1.4NA, Zeiss) which focuses the laser light on the sample. The fluorescent light is collected by the same objective. There is a 30 µm pinhole placed in the detection path to spatially filter the light. The emitted light passes an emission filter to remove any unwanted light from the excitation and a short pass filter of 770nm to remove any light from the AFM's laser. The resulting light is captured on the single photon avalanche photodiode (MPD-SCTC, PicoQuant) and the arrival times are determined and registered with a TCSPC Counter card (Becker&Hickl, SPC-830).

As discussed in 2.1.2: "Time Correlated Single Photon Counting", each laser pulse will, on average, result in much less than a single photon detection. A detection window of 50 ns is used, which is divided into 4096 channels (12,2 ps per channel). The time delay between the detected photon and the arrival of the next laser pulse

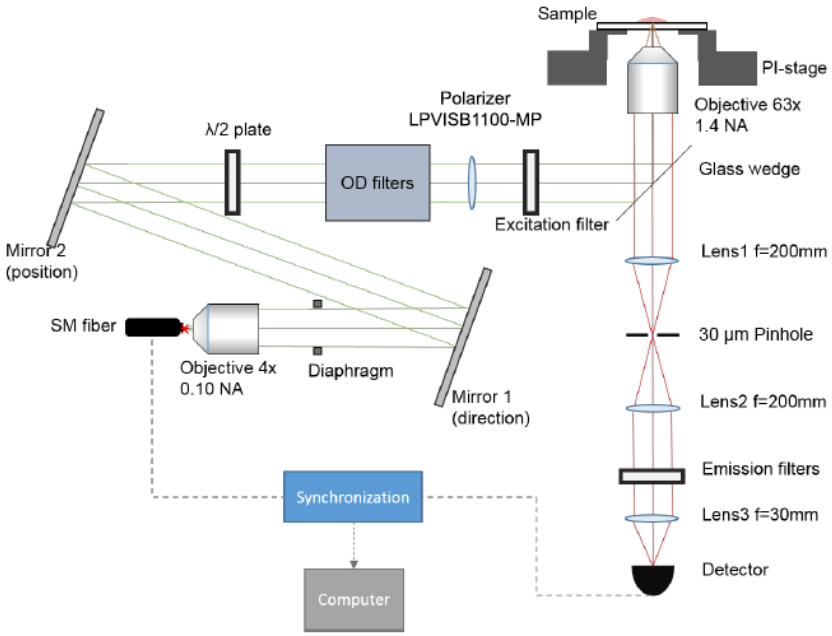

FIGURE 3.1: **Schematic of the optical components of our confocal microscope.** Green lines depict the excitation light, whereas the red ones show the emission. Adapted from *"Photonic emitter manipulation to achieve axial super-resolution for in vivo cell membrane topography studies"* [36].

is measured and used to calculate the emission time of the event. The collection of multiple photons can be used to plot a histogram of the arrival times, the lifetime can then be obtained by fitting this histogram.

The sample is placed on a XYZ piezo stage (P-527.3 CD, PI) which can move 200 µm in the X and Y direction, and 20 µm in the Z-direction, with an accuracy of 5 nm. The stage is controlled by a piezo controller (E-710, PI). The stage allows for the 2D scanning of the surface, moving the sample relative to the LDOS probe and the refocusing of the excitation laser.

Excitation and Emission Filters

Each fluorophore has its own characteristic absorption and emission spectra. The excitation wavelength and the filters therefore have to be specifically chosen to match the fluorophore's characteristics. In every setup for LDOS measurements a 770nm short pass filter is placed at the emission filter set to block out unwanted light from the AFM laser. The AOTF allows for a tunable excitation beam, which facilitates the use of different fluorophores over multiple experiments.

The filter set for both fluorophores (Rhodamine 101 & Rhodamine B) used in this study are similar. Both fluorophores are excited at 550 nm. The excitation filter is a 552/20 band pass filter, and the emission filter is a 590 long pass filter in addition to the short pass mentioned before. The setup has available filters for other fluorophores (for i.e. measurements on cell membranes), but these are not used in this study.

3.1.2 LDOS probe

As discussed in Chapter 2, the lifetime of fluorophores can be tuned using a metallic mirror. A gold coated polystyrene bead (Duke Standards, 100 µm in diameter with a 80 nm gold layer) was used for this purpose. In order to reliably control the distance of the mirror to the sample, it was attached to an in-contact AFM microcantilever (Bruker-MSCT) (Fig. 3.2) [26].

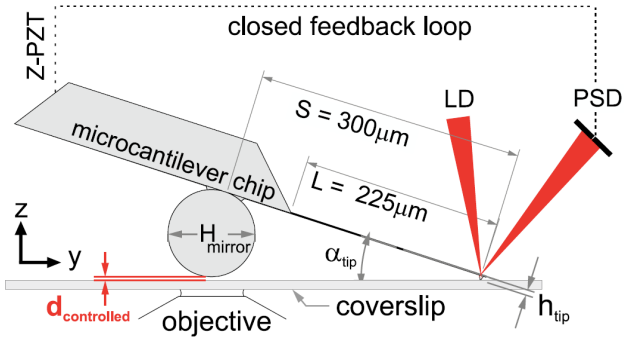

FIGURE 3.2: **Schematic of the LDOS probe.** A gold covered spherical bead is attached to a microcantilever. The microcantilever tip is brought into firm contact, and its deflection is measured by the reflected spot of the laser diode (LD) on the position sensitive detector (PSD). Due to a closed feedback loop, the distance between the mirror and the surface can be held constant. The angle between the surface and the microcantilever chip is α_{tip}. L is the microcantilever length. S is the distance between the mirror center and the microcantilever tip. H_{mirror} is the mirror diameter. h_{tip} is the tip height [26].

The spherical bead acts as a planar mirror since the size (100 µm) exceeds the size of the diffraction limited spot (300 nm) that is used to excite the fluorophores. A benefit of the spherical mirror is that the "flat" mirror will always be perpendicular to the surface irrespective of the angle α_{tip} that the cantilever makes with the surface.

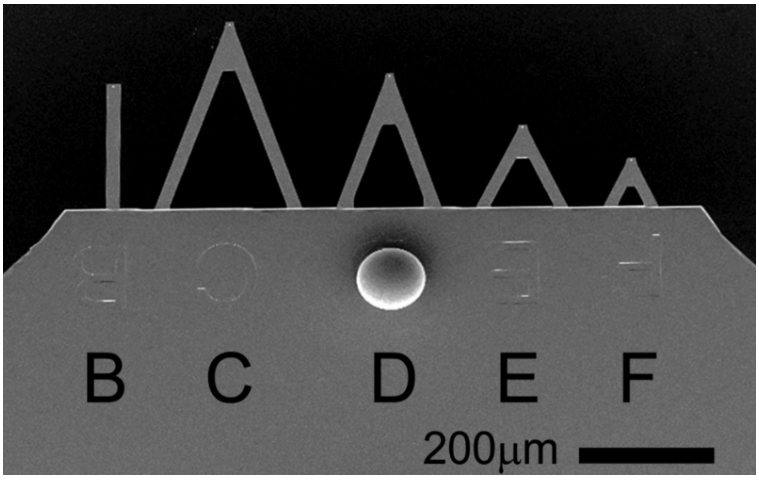

FIGURE 3.3: **SEM image of the microcantilever chip with the attached gold covered bead.** Cantilever D is used for LDOS related measurements.

The probe was fabricated by first attaching the polystyrene micro bead with a UV-curing glue (Norland Noa61) after which the glue is cured using a UV-LED (361

nm). The entire probe is then gold-sputtered on both sides at the Nanolab facilities (TCOathy, MESA+). The probe is sputtered on both sides to reduce the temperature response of the microcantilever.

The LDOS probe is controlled by familiar AFM technology and uses the angular deflection of laser light to control the mirror's position. The laser diode (LD, λ = 980 nm) is directed onto the tip of the cantilever, which reflects the laser light towards a position sensitive detector (PSD) (Fig. 3.2). When the cantilever is not in contact with the surface the measured deflection is zero. In contact however, the deflection changes due to the bending of the cantilever. The deflection, and thus the height of the probe relative to the surface, can be held constant through a closed feedback loop. This feedback loop is used to keep the probe at a constant axial position when scanning the surface with an accuracy of 3 nm [26]. It is important to note that the AFM feedback will only compensate for first order changes over the surface. If the surface is stressed in such a way that it arches, the curvature is not corrected by the AFM feedback and this can lead to poor measurements.

This entire system needs to be calibrated before use to determine the absolute distance between the mirror and the sample.

Probe-Distance Calibration

The absolute distance between the gold mirror and the surface is calibrated by moving the piezo stage in the z-direction in a predetermined manner. First the stage drops 1.2 µm at a constant speed where after it returns to its original position. Using this movement, the relationship between the AFM laser deflection and piezo-stage movement becomes evident.

Probe-Focus Alignment

After the probe is placed close to the surface with the AFM feedback keeping it in place, the probe can be placed exactly above the focal spot of the excitation laser. This is done by moving the AFM relative to the focal spot. Initially the base on which the AFM is placed can be moved slightly, for the final alignment fine knobs are used (Fig. 3.4). Since the gold mirror is close to the glass surface, interference patterns become visible which can be used to laterally align the probe with the focal spot. By slightly moving the objective, aligning the reflection on both the glass substrate and the gold mirror concludes the probe alignment.

After the probe is aligned laterally, the stage is raised in such a way that the gold mirror is in slight contact with the surface. This contact is easily visible when looking through the eyepiece and is also seen on the AFM deflection signal. From the deflection signal a contact distance can be set before continuing experiments.

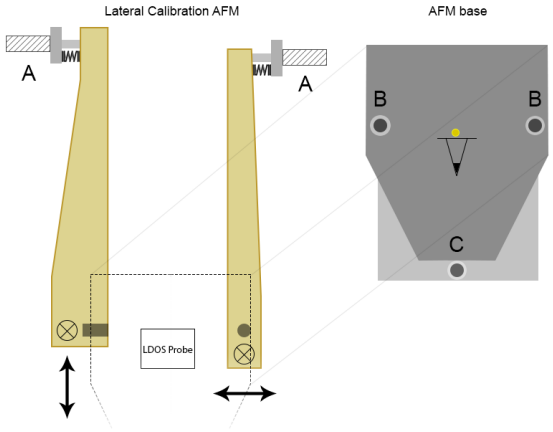

FIGURE 3.4: **Schematic of components used to align the LDOS probe.** (Left) The base of the AFM is positioned on two large levers. Using two fine knobs (A), the LDOS probe can be aligned laterally with high accuracy. (Right) The initial axial positioning of the LDOS probe is done by turning the knobs on the AFM base. The knobs close to the cantilever (B) will cause a large drop of the probe, while the knob far from the cantilever (C) will cause only a slight drop of the probe.

Aligning topography features

In this study, measurements were performed on several non-flat surfaces. These were designed in such a way that the AFM tip would still be in contact with a flat surface to insure a constant control feedback. The features include step gratings of varying depths from 5 up to 100 nm. A grating consisted of six indentations which were spaced 10 µm apart. Five groups of gratings were etched into the glass 500 µm apart. In the end the structures covered roughly 2 by 2 mm. The features are so small they are hardly visible to the eye, so aligning the structures with the laser and mirror requires additional steps.

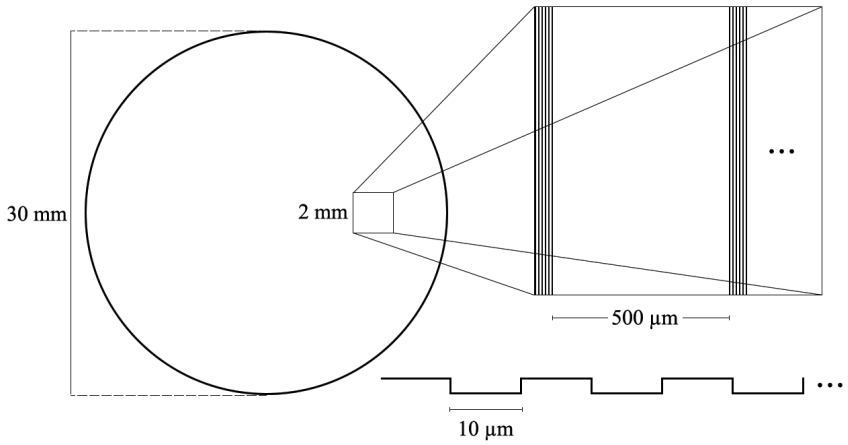

FIGURE 3.5: **Schematic of a coverslip with etched gratings.** Gratings are etched into a coverslip with varying depths. The gratings are spaced 500 µm apart. This space between the gratings assures that the AFM tip is always in contact with a flat surface.

To facilitate the alignment of the features with the laser focus, an alignment plate was designed for both the LDOS setup and a dark field microscope. The dark field microscope has the benefit of high contrast, making it far simpler to find the scattering edges of the etched gratings. The alignment plate, which is placed between a light source and the sample, comes into play to connect both microscopes. The alignment plate consists of a thin metal plate with two slits: one vertical and one horizontal. The illumination of the alignment plate on the sample (or sample holder) can then be marked and used to roughly align the sample under the LDOS setup.

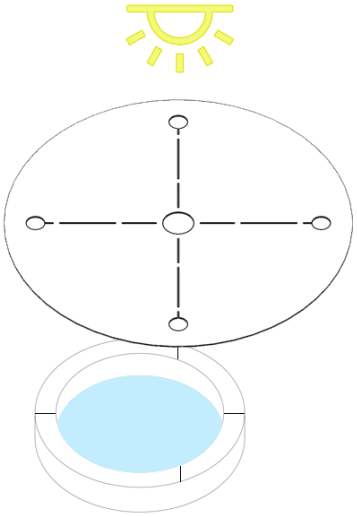

FIGURE 3.6: **Schematic of the alignment plate procedure.** When the alignment plate is illuminated, the passed light falls on the sample. These lines can be marked on the sample, or sample holder. The LDOS set-up includes a similar setup; aligning the passed light with the markings gives a rough alignment of the feature.

To finalize the alignment, we use the excitation laser carefully. By defocusing the laser and increasing its intensity we can still see the defocused spot. When this defocused spot overlays with the grating, scattering from the grating edges, showing clear lines in the grating orientation, become visible. Once the interference patterns become visible the gratings are aligned with the laser focus and LDOS probe, and experiments can be performed on the step features.

Measurements in aqueous environment

In order to mimic the conditions of actual cells, measurements were also performed on lipid bilayers. These bilayers were submerged in an aqueous solution which require additional measures. Since the aqueous medium needs to be contained, the sample substrates are placed in a small sample holder (Bioptechs 10 mm Interchangeable Coverslip Dish (40 mm Base)). The sample is secured by a plastic ring and rubber band, which tightly secures the contact with the substrate to prevent leakage. Additionally, the water level must reach the prism of the AFM head. If the water level would be lower or higher than this, the additional surface diffraction would disturb the measurements (Fig. 3.7).

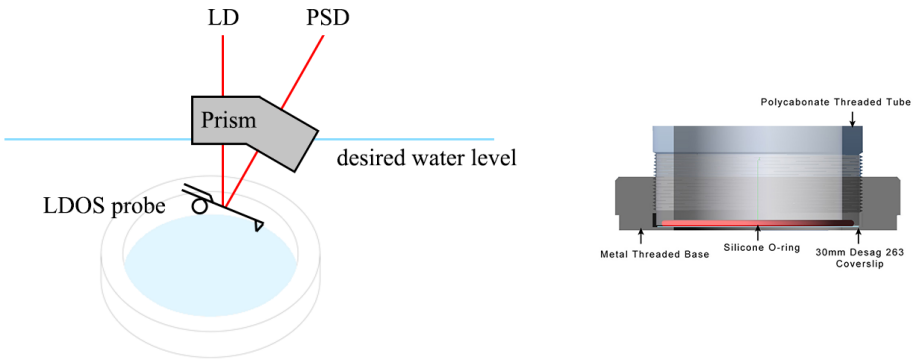

FIGURE 3.7: **Measurements in an aqueous environment.** (Left) Measurements in an aqueous medium are performed in a sample holder, which contains the medium. The water-air interface must be carefully aligned with the prism to prevent additional diffraction of the AFM laser diode. (Right) The sample holder consists of a polycarbonate cylinder that is screwed into a metal base. The sample is secured by a silicone O-ring to assure a watertight seal. [37]

3.2 LDOS Nano-ruler Concept

With the LDOS probe we can manipulate the lifetime of fluorophores by varying the position of the mirror. The LDOS nano-ruler uses the measured lifetimes to calculate the distance between the mirror and the surface.

Consider a non-flat fluorophore-covered surface (Fig. 3.8). Initially, the mirror can be lowered in a controlled manner, eventually touching the surface. During this process, the relation between distance-to-mirror and lifetime is registered (the $\tau(d)$ calibration curve). We can then start the scan by positioning the mirror at a fixed distance, h. As the surface is scanned, the changing distance-to-mirror, d, will produce a changing lifetime. Using the calibration curve, we can calculate the distance-to-mirror, and reveal the topography.

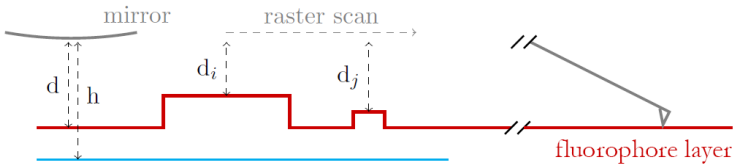

FIGURE 3.8: **Schematic of the LDOS scan procedure over a surface.** The mirror is positioned at a fixed height h. As the probe scans the surface, the measured lifetime will vary depending on the mirror-to-surface distance d. Where the cantilever touches the surface, the sample is completely flat [36].

3.3 Sample Preparation

In this section we introduce the methods used to fabricate a multitude of samples. Initial experiments were performed on fluorophores embedded in polystyrene, whilst later experiments were measured on a lipid bilayer to better mimic the cell

membrane and improve stability of the system. A glass coverslip (Bioptechs Inc. 30 nm Coverslips 1.5 Thick) was used as substrate unless stated otherwise.

There are some requirements that the sample must fulfil. The deposited layer must be thin and homogeneously distributed. A thin layer will minimize the distance distribution between the fluorophores and the LDOS probe, and therefore minimize the lifetime distribution from a single point measurement. The layer however must be fabricated in such a way that there is still enough fluorescent light available for practical measurements. Furthermore, the fluorophore concentration must not be so high as to lead to quenching between the fluorophores. The orientation of the fluorophores is also a consideration since this is an important factor in the lifetime modulation.

3.3.1 Polystyrene

A previous study [36] has shown that spin-coated fluorophore-embedded polystyrene is highly suitable for the set of experiment we want to perform. It does not dissolve in water, which allows us to measure in more physiological conditions. It also shows a better homogeneity in terms of lifetime when compared to PVA, which is traditionally used to embed fluorophores.

Rhodamine 101 (Rh101) was used as the fluorescent dye in polystyrene since it has been used in previous studies using the LDOS probe. Therefore, we know what to expect from the lifetime modulation measurements. Rh101 has an absorption peak at 568nm and an emission maximum at 589nm.

In order to fabricate the thin Rh101-embedded polystyrene layer which fulfilled all requirements 10^{-7} M Rh101 was embedded in 0.2 % w/v polystyrene. 50 µL of this solution was consequently spin coated on a glass substrate at 6000 rpm for 1 minute. The resulting layer had a thickness of roughly 10 nm.

3.3.2 Lipid Bilayer

In order to mimic a more physiological environment and reduce the AFM-tip interactions, lipid bilayers were deposited on a glass substrate. In order to keep the supported bilayer stable it had to be continuously immersed in water. There are several techniques that have been put to use in order to create a stable, largely homogeneous layer. For flat surfaces, vesicle deposition was a simple and easy-to-perform method. However, for covering non-flat surfaces, attempts were made to cover the substrate by dipcoating and Langmuir-Blodgett deposition.

The lipid composition consisted of a 1:100 ratio between the fluorophore-bound lipid and the non-bound lipid. This ratio leads to a sufficient number of emitted photons whilst excluding any notable quenching between the fluorophores. The main non-bound lipid component that was used is DOPC (1,2-dioleoyl-sn-glycero-3-phosphocholine, Avanti Polar Lipids). For the fluorescently labeled lipids, DOPE (1,2-dioleoyl-sn-glycero-3-phosphoethanolamine) was head labeled with Rhodamine B.

Vesicle deposition

Solid-supported lipid bilayers can be formed by exposing small lipid vesicles to a hydrophilic substrate. After the vesicles are absorbed to the surface, they can be ruptured

Once a vesicle has ruptured, the edges of the resulting bilayer patch are exposed. These edges are energetically unfavorable which promotes the interaction with adjacent patches. With a sufficient density of vesicles, these will form extended bilayer patches [38].

For protocol see Appendix B.1: "Protocol: Vesicle Deposition".

Dipcoating

When an insoluble film forms on the air-water interface it is usually one molecule thick, since this arrangement is entropically favorable. Such a film is called a insoluble monolayer and the lower bulk phase is called the subphase. Passing a solid substrate through the monolayer can cause the monolayer to deposit on the substrate. This can be repeated multiple time to deposit additional layers on the surface.

In order to create the monolayer the lipids were dissolved in chloroform. Drops of the volatile solution are placed on the surface and since chloroform has a positive spreading coefficient, it will quickly cover the subphase. The solution spreads, the solvent evaporates, and the monolayer is left [39].

For protocol see Appendix B.1: "Protocol: Dipcoating".

Langmuir-Blodgett Deposition

Langmuir-Blodgett (LB) Deposition is similar to dipcoating, but the monolayers are manipulated on a surface film balance, also called a Langmuir trough. A Langmuir trough consists of a shallow trough with hydrophobic edges and barriers, and an electronic device to measure the surface tension (Fig. 3.9).

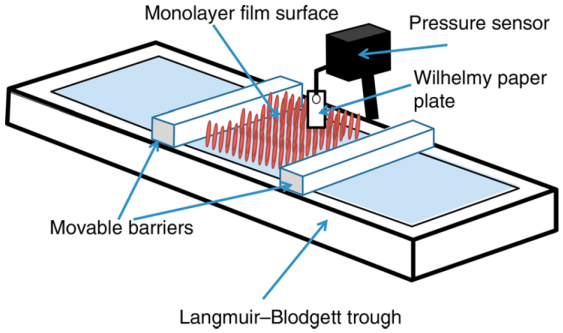

FIGURE 3.9: **Schematic of a Langmuir-Blodgett through [40].**

The trough is slightly overfilled with water so that the barriers can divide sections of water surface. The monolayer is spread by adding drops of chloroform-lipid solution of known concentration. After the chloroform has evaporated, the monolayer can be compressed or expanded by sliding the barrier along the trough edges.

The surface tension is measured by a Wilhelmy plate hanging through the surface. The basic experimental result is then an isotherm of surface pressure against area (either the area between the barriers or molecular area). From these isotherms it is possible to recognize several principal monolayer phases such as a gaseous, liquid-expanded, liquid-condensed and a solid phase.

For satisfactory deposition, the surface pressure should be sufficiently high for the monolayer to be in a liquid-condensed state. An automated system moves the barriers to maintain a constant surface pressure are the film is deposited on the substrate. This ensures that the monolayer remains condensed at all times [39].

For protocol see Appendix B.1: "Protocol: Langmuir-Blodgett Deposition".

Chapter 4

Reproducibility of the Lifetime-Distance Curve

Since the lifetime-distance ($\tau(d)$) curve is essential to compute the topography of the measured surface, it should be validated. In this chapter, we study the reproducibility of the $\tau(d)$ curve under different circumstances.

4.1 Influence of Intensity on the Lifetime-Distance Curve

To begin with it should be clear that the mirror does not only has an influence on the lifetime of the fluorophore, but also on the amount of photons (counts) the fluorophore will emit. Although the lifetime is count independent, more counts will lead to a better fit of the TCSPC data and a reduced error in the determination of the lifetime.

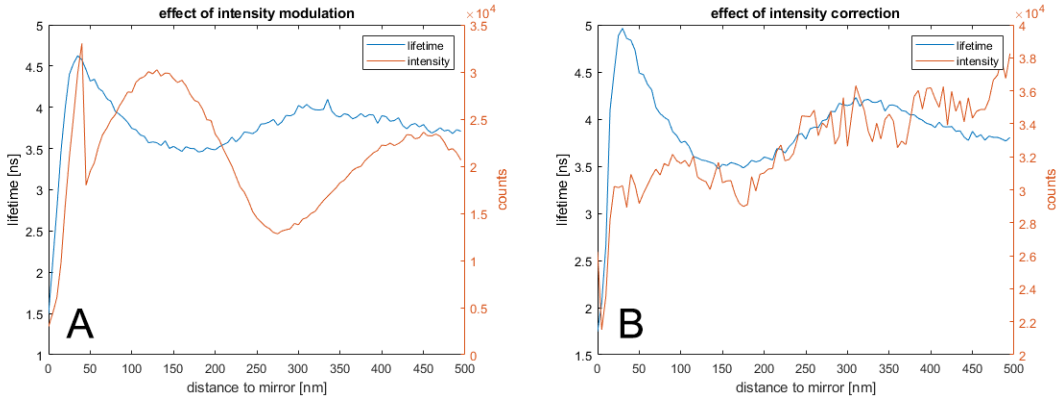

FIGURE 4.1: **Effect of intensity on lifetime accuracy.** A) A $\tau(d)$ curve that is solely corrected on the last 50 nm. B) Normalizing for intensity provides a more regular $\tau(d)$ curve.

When measuring a $\tau(d)$ scan, early experiments simply doubled the collection time of the last 10 points (50 nm respectively), where the loss of intensity is most notable (Fig. 4.1 A). Later experiments however implemented a normalization for intensity which allowed for a more constant number of counts across all distances (Fig. 4.1 B). Experience shows that $2 \cdot 10^4$ counts are sufficient for lifetime measurements and was set as a minimal for topography analysis (see section 5.2 Experimental Determination of the Axial Resolution).

4.2 Reproducibility on a Polystyrene Layer

4.2.1 Thickness

The thickness of a polystyrene layer influences the modulated lifetime. Early experiments were performed on a polystyrene layer of roughly 14 nm thick, while later experiments were performed on thinner samples of roughly 10 nm thick. Since fluorophores are spread throughout the layer, influence of the mirror will not give rise to a single lifetime, but rather a distribution of lifetimes. We still assume a "monolayer" principle when using a single exponential to fit the TCSPC data. But as one can imagine, a thinner layer will have a more uniform lifetime compared to the thicker sample. The thinner layer will therefore show higher peaks in the $\tau(d)$ curve (Fig. 4.2).

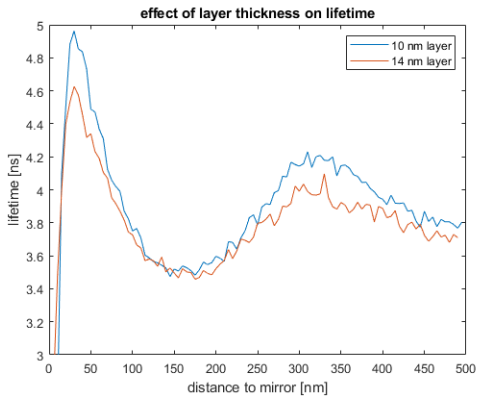

FIGURE 4.2: **Effect of Polystyrene Layer Thickness on the $\tau(d)$ curve.** Thinner layers will produce more extreme peaks and valleys.

Since the thinner layer has higher peaks in the $\tau(d)$ curve, the slopes are consequently more steep. This increased steepness will improve the differentiation between distances to the mirror and lead to better topography measurements.

4.2.2 Polysterene Measurement over a Step

The nano-ruler principle only works when the $\tau(d)$ curve is identical across the measured surface. This assumption is compelling when discussing flat spin-coated surfaces. For non-flat surfaces this is not evident. As we have seen in the previous section, a few nanometer difference already has a significant effect on the lifetime modulation in polystyrene layers.

To check if polystyrene is suitable to cover non-flat surfaces, the surface is checked before and after the spin-coating process by an Atomic Force Microscope (AFM).

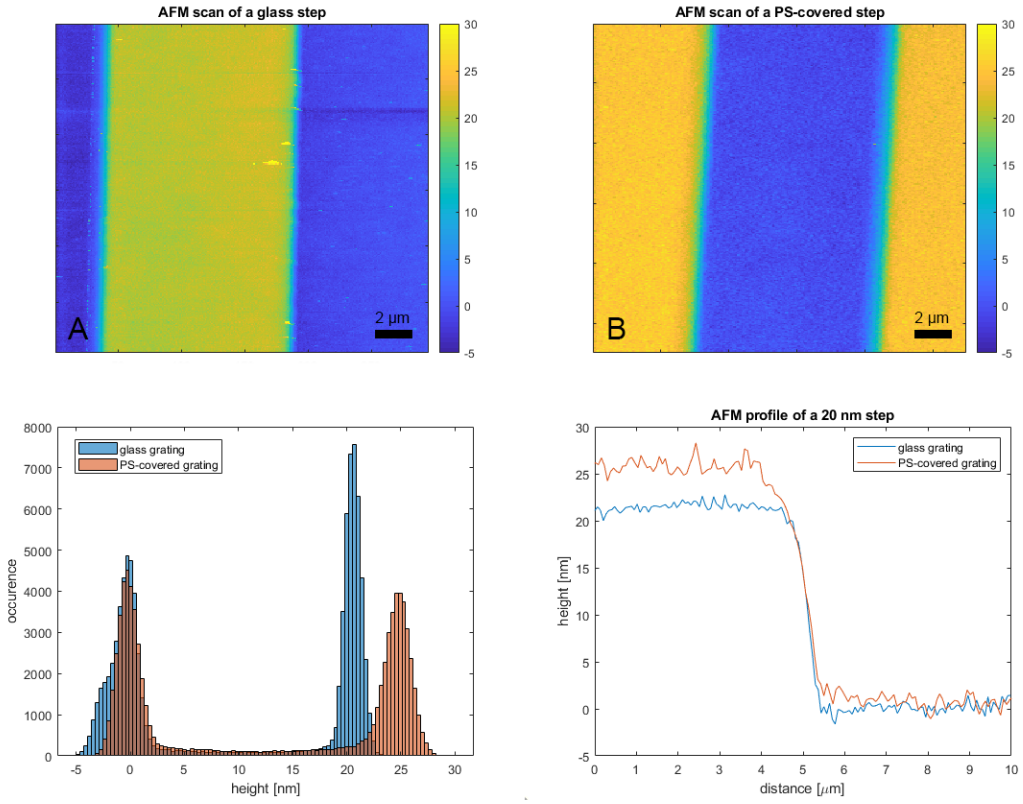

FIGURE 4.3: **AFM image of a nanometer step, before and after spin-coating.** (A) An AFM image of a ∼20 nm step. (B) An AFM image of a ∼20 nm PS-covered step. (C) A histogram comparing the difference in heights. The PS-covered step seems to have increased significantly due to a difference in layer thickness. (D) Perpendicular profiles of the two samples illustrates that the PS coverage is gradual over the step.

From the AFM measurements we can conclude that this particular glass etched step (Fig. 4.3) is roughly 23 nm. However, after spin coating the sample, the step size has increased to 25 nm. This suggests that the layer on the lower section is thinner compared upper layer. The step is also no longer abrupt, but it seems a gradient appears due to the polystyrene coverage.

When we measure this sample with the LDOS system, we can see what these layer effects have on the final result. The $\tau(d)$ curves are dissimilar as we have already previously observed (Fig. 4.2). As a result, the conversion of lifetime to distance is only strictly valid on the side which calibration $\tau(d)$ curve is used. For this simple binary system, the conversion has been done with both calibration curves (Fig. 4.4).

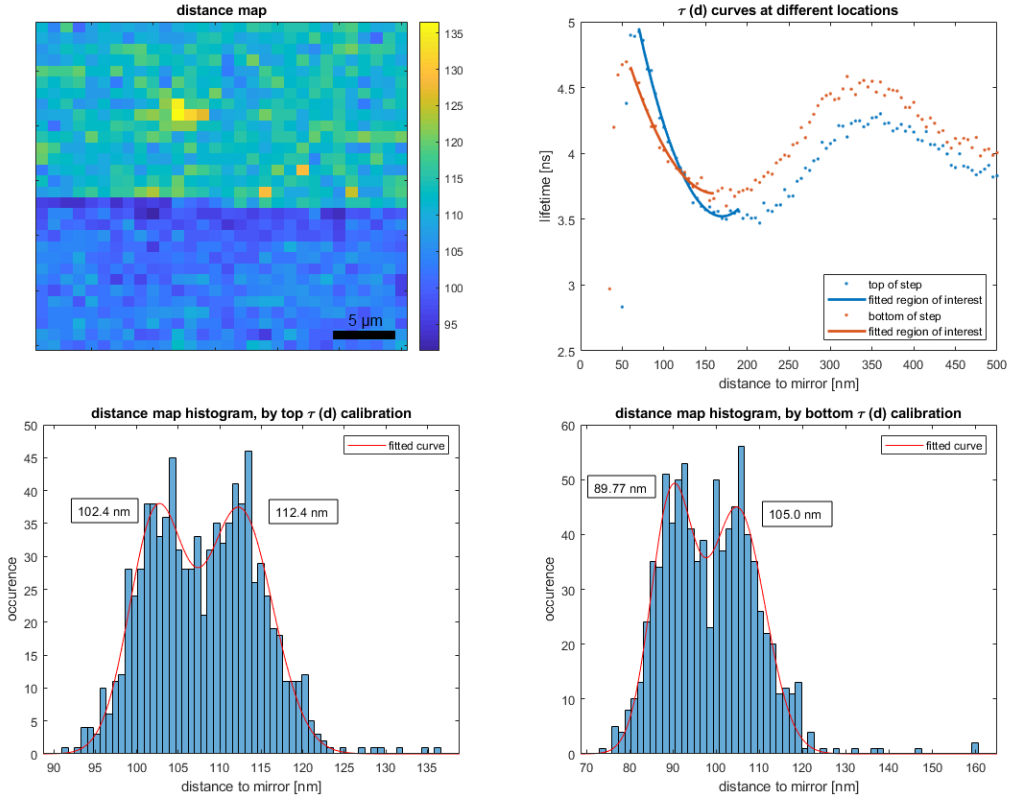

FIGURE 4.4: **The Effects of Layer Thickness on a Step Feature.** Due to the difference in layer thickness, each side of the step has a different $\tau(d)$ curve. This difference makes it difficult to properly resolve the feature.

To overcome the inconsistency of multiple $\tau(d)$ curves, the piezo stage can be used to mimic a nanometer step. By performing a topography scan on a flat surface, whilst dropping the piezo stage halfway through the measurement, a step can be imitated. This ensures that the $\tau(d)$ calibration curve is valid for the entire sample.

The mimiced step missed the actual step component over which fluorophores could also be deposited. Compared to the etched step sample however, the flat surfaces are absolutely similar and since we are scanning large surface areas, the total step measurement is still comparable.

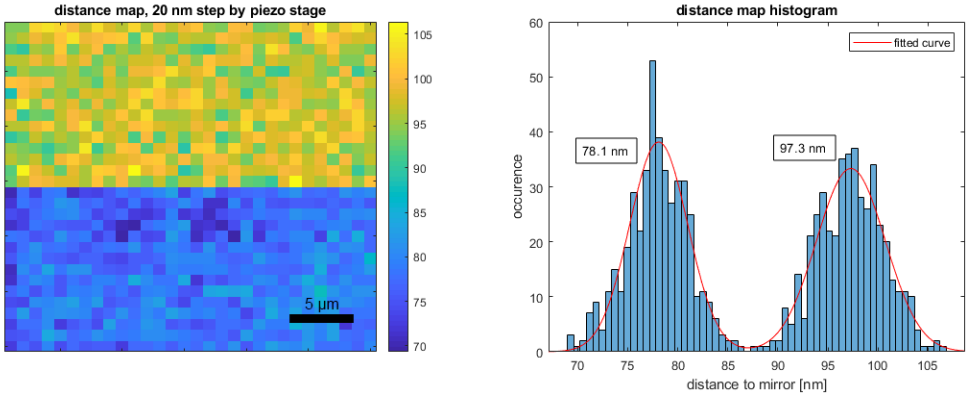

FIGURE 4.5: **A mimicked step using the piezo stage.** Performed step: 20 nm, measured step: 19.2 nm.

4.3 Reproducibility on Lipid Bilayers

Lipid bilayers were deposited on a glass substrate to mimic a more physiological environment and eliminate the layer effects that occur with the polystyrene sample. Another benefit of a lipid bilayer is the homogeneity of the fluorophore distribution and the uniqueness of its composition (see section 3.3.2: "Lipid Bilayer").

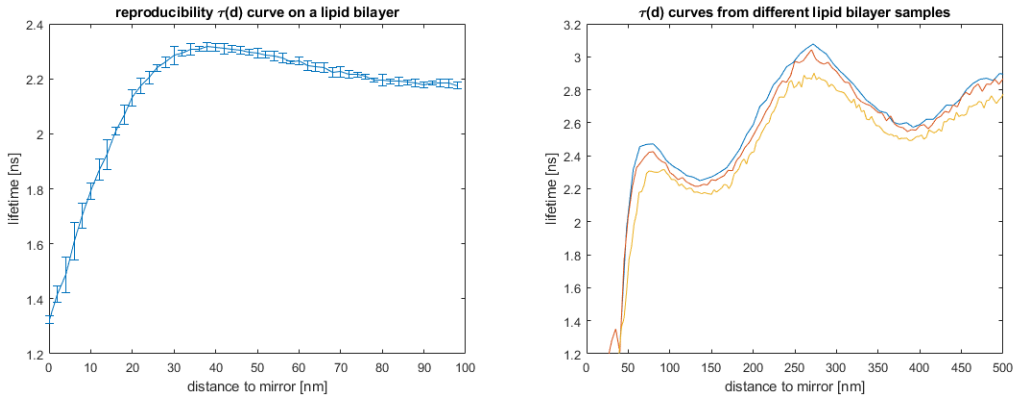

FIGURE 4.6: **Reproducibility of $\tau(d)$ curves on lipid bilayers.** (Left) Reproducibility of the $\tau(d)$ curve on a single sample location. Errorbars represent the standard deviation of 8 measurements. (Right) $\tau(d)$ curves look different between samples, most likely due to a difference in sample preparation.

Even though a lipid bilayer is far more consistent than polystyrene in theory, the $\tau(d)$ curves from different samples still show discrepancies between each other. The majority of this discrepancy is most likely due to a difference in sample preparation, specifically the lipid concentration.

4.4 Instrumental Influence

There are several instrumental influences on the lifetime that should be minimized whenever possible. Most notable are the interaction between the AFM tip and the surface, and the proper alignment of the probe.

4.4.1 AFM-Surface Interaction

The AFM feedback is used to keep the gold mirror at a fixed position. However, there will always be fluctuations within the system. There is a very notable difference between surface coverage as can be seen in table 4.1. The difference due to the polystyrene layer is most probably due to the soft nature of the material (see Appendix A: "AFM-PS Interaction"). The lipid bilayer seems to have little to no additional effect on the cantilever.

Surface Coverage	Peak-to-Peak [nm]
Glass Substrate	3
Polystyrene	8
Lipid Bilayer	3

TABLE 4.1: **The cantilever jitter caused by the feedback loop.**

4.4.2 Lateral Alignment of the Probe

Another element that can have an effect on the $\tau(d)$ curve, is the lateral alignment of the sphere over the focal spot. Typically, the probe is aligned within 0.2 µm of the focal spot. During experiments, probe misalignment (> 1 µm) occurred rarely and was quickly corrected. However, it is interesting to see the effects on the $\tau(d)$ curve, which mainly situate around the first section of the curve.

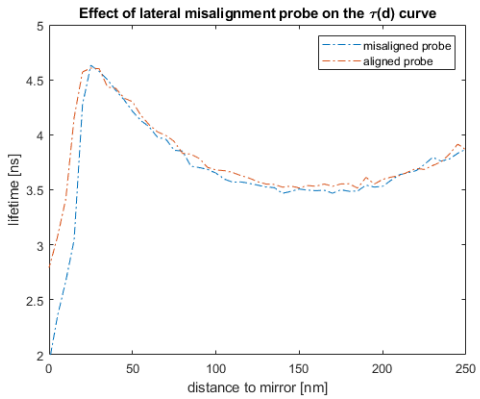

FIGURE 4.7: **The effect of roughly 1 µm lateral misalignment of the LDOS probe on the $\tau(d)$ curve.**

4.5 Discussion

Although polystyrene samples are easy to fabricate, their interactions with the AFM tip and the uneven distributions over topography features makes them unsuited for characterizing the the LDOS nano-ruler.

This becomes more evident in figure 4.4. Here we have scanned an unevenly covered PS step surface. We have used both calibration curves to display the differences between determined step sizes. One would expect however, that these are correct for their respective surfaces. Closer inspection reveals otherwise, subtraction from the determined distances reveals a step size of 2.6 nm (105.0 - 102.4). When trying to overlap the $\tau(d)$ curves, which should also give a rough estimate of the step size, the curves have to be displaced by 15 nm. It is unclear why these differences are so significant, but it becomes increasingly clear that polystyrene surfaces are unsuited for topography measurements.

We have briefly considered the effects of the AFM feedback and jitter. Although these effects decrease the "purity" of the lifetime, the nano-ruler concept is still valid. Vibrations that will change the perceived lifetime during the $\tau(d)$ measurement will also arise during surface measurements. Reducing these effects however, will increase the steepness of the curves, similar to what happens when we coat a thinner polystyrene layer (Fig. 4.2), and lead to a higher obtainable resolution.

Chapter 5

Determining the Axial Resolution

The LDOS nano-ruler can theoretically obtain a very high resolution. In this chapter, we will attempt to determine this resolution and how it is influenced by the slope of the $\tau(d)$ curve and number of detected photons.

5.1 Methodology

To determine the axial resolution of the LDOS nano-ruler, the definition of resolution was used as starting point. The resolution of an optical microscope is defined as the shortest distance between two points that can still be distinguished as separate entities. A generally accepted criterion of this distinction is the Rayleigh criterion, which considers the overlap of Airy disks. In a similar fashion, we define our axial resolution as the Full Width Half Maximum (FWHM) of our distance distribution.

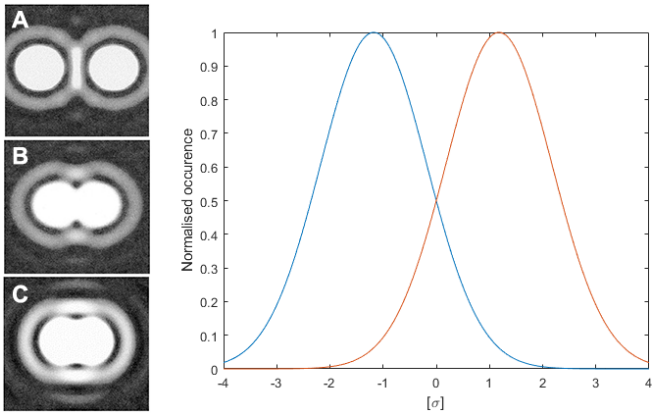

FIGURE 5.1: **Definitions of Resolution.** On the left, distinguishing two airy disks is a typical measure for optical resolution. As the disks come closer, the intensity dip between them becomes smaller. [41] On the right side, two similar normal distributions are separated by their Full Width Half Maximum.

The FWHM is determined by the following steps:

1. Measure lifetimes over a flat surface
2. Translate the lifetimes into distances using the $\tau(d)$ curve
3. Check for normal distribution
4. Calculate the FWHM from the standard deviation

The surface needs to be flat in order to maintain a constant distance between the surface and the mirror. The distribution is then checked for normality after the translation to distances. This encapsulates effects that occur due to the non-linearity of the $\tau(d)$ curve at certain distances. If the distribution is a normal distribution, the FWHM can be calculated by the following equation (See Appendix C "Derivation of the Full Width Half Maximum of a Normal Distribution" for the derivation):

$$FWHM = 2\sqrt{2 \cdot ln(2)} \cdot \sigma \approx 2.355\sigma$$

5.2 Experimental Determination of the Axial Resolution

The axial resolution is not only dependent on the slope of the $\tau(d)$ curve, but also the number of photons that are collected and used for the fit. To get a better understanding into this effect the number of photons that are used for the fit can be limited. This limitation was set to use the first x number of photons, by increments of 1000. Per surface scan, 400 measurements are performed (20x20) with a lateral scanning step of 300 nm.

5.2.1 Polystyrene

Initial experiments were performed on the polystyrene covered surface. Surface scans to calculate the achievable axial resolution were performed on various points within the first 3 regions. The first region however proved difficult to scan, displaying non-normal lifetime distributions. The processed data from region II & III is displayed in figure 5.2.

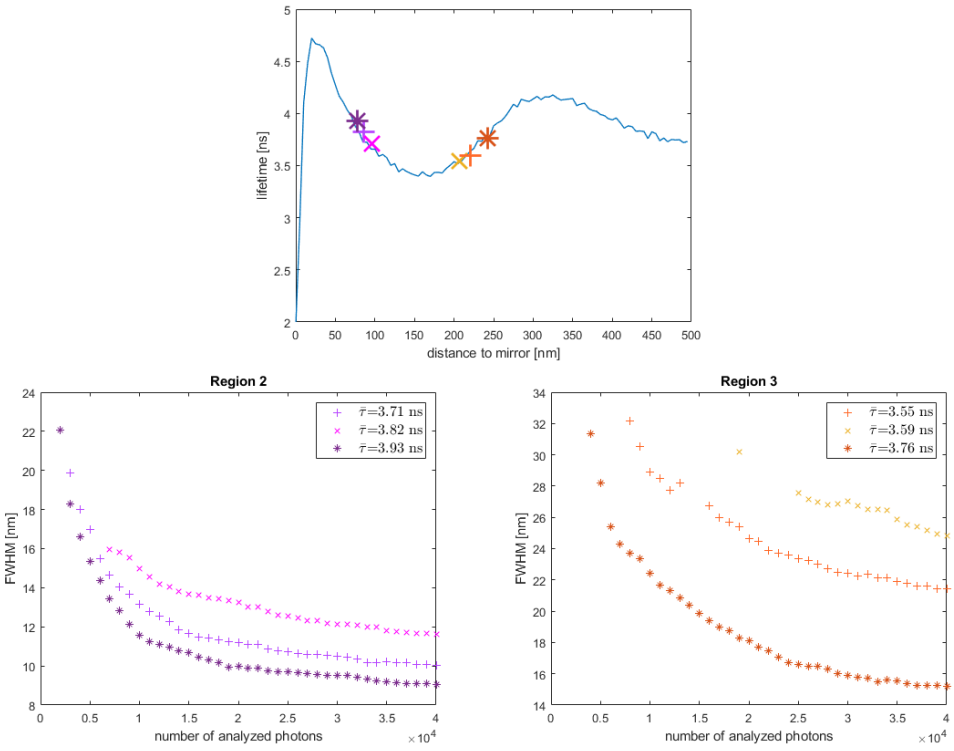

FIGURE 5.2: **Axial resolution measurements on a polystyrene sample.** The top figure shows a $\tau(d)$ curve with the measured locations. The bottom figures show the corresponding FWHM versus number of analyzed photons. More photons lead to a higher obtainable resolution.

Because the regions are not linear, there is a difference between obtainable resolutions in a single region. This effect is quite significant in region III (see table 5.1). The slopes were calculated by fitting a second-order polynomial to the region, followed by analytically determining the slope at the point of interest.

Distance to mirror [nm]	**Lifetime [nm]**	**FWHM [nm] at $20 \cdot 10^3$ photons**	**Slope [ps/nm]**
77.6 (∗)	3.93	10.0	13.8
86.0 (+)	3.82	11.2	11.3
96.1 (×)	3.71	13.3	9.2
207.3 (×)	3.55	30.2*	5.2
220.1 (+)	3.59	24.7	6.2
242.7 (∗)	3.76	18.1	7.5

TABLE 5.1: **Resolution on a polystyrene sample at $20 \cdot 10^3$ counts.**

5.2.2 Lipid Bilayer

On a lipid bilayer surface, scans were performed in region I and III.

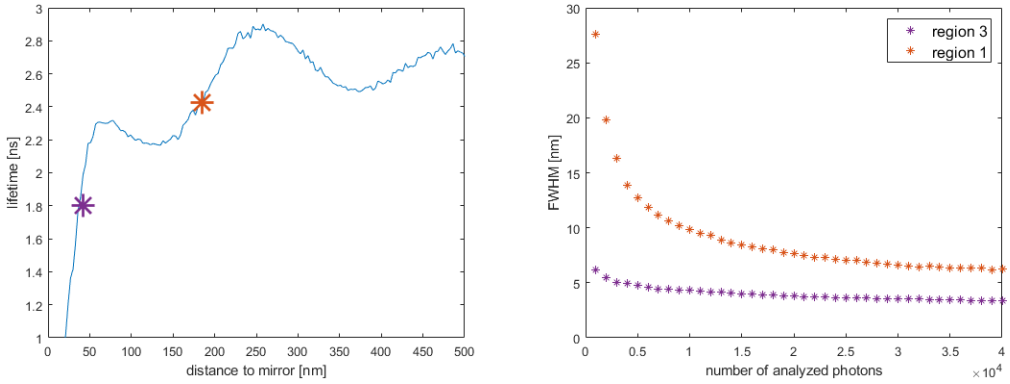

FIGURE 5.3: **Axial resolution measurements on a lipid bilayer sample.**

Distance to mirror [nm]	Lifetime [nm]	FWHM [nm] at $20 \cdot 10^3$ photons	Slope [ps/nm]
42.5 (∗)	1.80	3.8	35.2
184.8 (∗)	2.43	7.6	8.1

TABLE 5.2: **Resolution on a lipid bilayer sample at $20 \cdot 10^3$ counts.**

The lipid bilayer sample provides a considerably lower FWHM when compared to the polystyrene layer. Even at comparable slopes, the lipid bilayer has a significantly lower FWHM. It also seems that fewer photons are required to achieve an accurate fit. Whereas measurements on polystyrene would require $20 \cdot 10^3$ photons to determine an accurate lifetime, the lipid bilayer sample only requires $10 \cdot 10^3$ or even fewer photons. This means that generally, measurements on lipid bilayer are not only more accurate, but can also be performed faster.

These benefits are most likely owed to the composition of the lipid bilayer. The more uniform lifetime distribution and reduced instrumental effects (see section 4.4.1 AFM-Surface Interaction) seem to greatly increase the axial resolving power of the LDOS nano-ruler.

5.3 Calculating the Axial Resolution Through Simulations

Simulations were performed to get a first indication of the development of the axial resolution over different mirror distances. This could give some insight into which areas measurements are useful, not only in terms of resolution, but also in terms of the working range in which measurements are possible.

TCSPC data was simulated by a single exponential probability distribution, in which the lifetime was selected from a smoothed $\tau(d)$ curve (using a Savitzky-Golay filter). Per single instance $20 \cdot 10^3$ photons were generated. The algorithm used non-linear least squared curve fitting to determine the lifetime of an instance. Similar to experiments, 900 instances were generated of which, the standard deviation, and the FWHM were calculated.

In the experimental setting, a slope was fitted with a polynomial to translate lifetime into distance. For the simulations, a large part of the entire $\tau(d)$ curve was fitted with a ninth degree polynomial. Instead of directly translating the lifetimes into distances, tangent lines were analytically determined and used for translation.

This is necessary because lifetime distributions around extrema can fall outside the range of the $tau(d)$ curve (e.g. a lifetime of 2.5 ns at 75 nm).

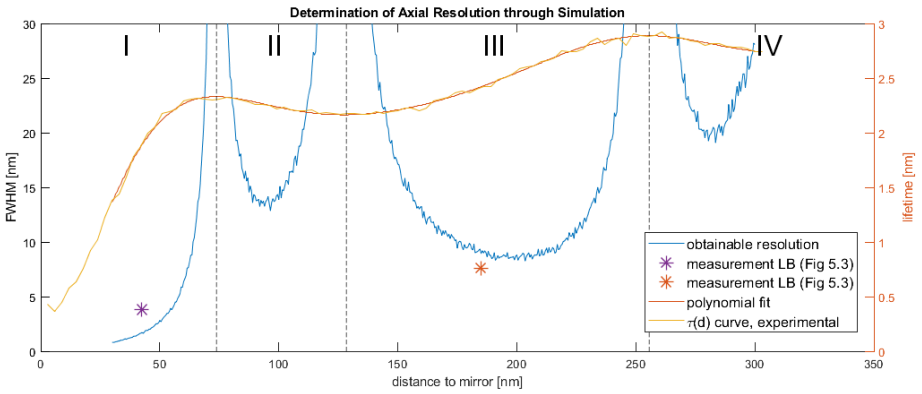

FIGURE 5.4: **The simulated values of the FWHM as measure for resolution on a lipid bilayer at $20 \cdot 10^3$ counts.** As the $\tau(d)$ curve (orange) begins to flatten, the resolution quickly becomes infinitely large. This sections the curve into regions which are accessible for practical measurements. The asterisks mark the calculated values from experiments (Fig. 5.3).

As one would expect, when the $\tau(d)$ curve flattens, the achievable axial resolution quickly becomes unsuitable for membrane imaging. This is what sections the curve into the aforementioned regions.

Region I shows great potential with regards to resolution. However, being close to the measured surface is accompanied with certain risks. Therefor the practical measuring range should not be accepted as starting from 0 nm. Taking this into account, the workable range lies roughly between 25 and 65 nm.

Region II has a extremely narrow working range due to the flatness of the $\tau(d)$ curve. Measurements seem only to result in an acceptable resolution between 80 and 110 nm.

Region III shows a fairly constant resolution over a large distance range. Practical measurements between 150 and 245 nm seem possible.

5.4 Discussion

In this chapter the axial resolution was determined by defining it as the Full Width Half Maximum of our distance distribution. However, the $\tau(d)$ calibration curve is non-linear, and as we have seen in both experiments and simulations, resolution is also dependent on the distance to the mirror. This in return then influences our ability to discriminate heights in our measurements.

Consider figure 5.5, due to the different distributions the ability to discern the two points is not equal to either FWHM, but rather to the average of both. So, if FWHM_1 = 20 nm, and FWHM_2 = 10 nm, we are able to differentiate these points when they are 15 nm apart.

Essentially this means that every point on the $\tau(d)$ curve has an effective downward resolution, and upward resolution, depending on their neighboring slopes.

When performing experimental measurements in this chapter, the probe was carefully positioned in the middle of a region. When moving to more practical measurements, such as on cell membranes, the mean distance to the mirror should also

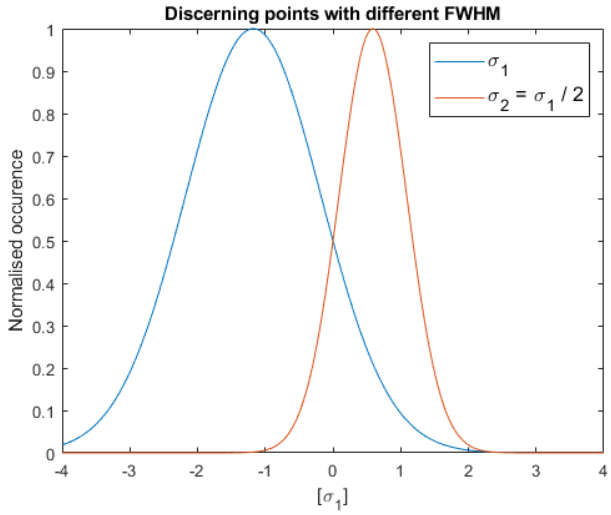

FIGURE 5.5: **Discerning two points with different distance distributions.**

be centered in a region as to provide the best resolution and largest working range. This probe-region centering would be an additional calibration step for every surface measurement since the surface topography is initially unknown.

Consider figure 5.6, although the left probe is located at an ideal position (red dashed line) to measure locally, it is sub optimal for the entire surface. An initial measurement needs to be performed to determine the mean distance to the mirror, and to optimize the probe position for the final scan (right probe).

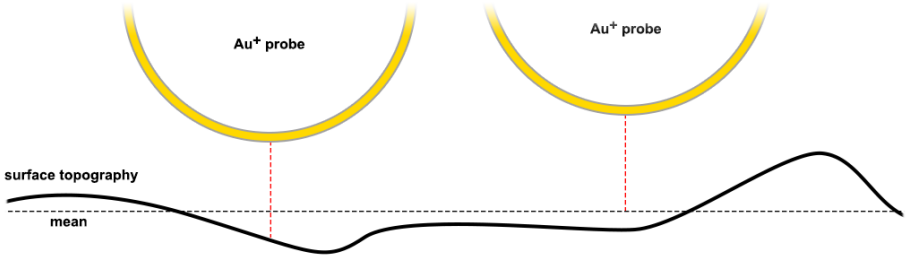

FIGURE 5.6: **Optimizing the probe position improves the axial work range and resolution.** (Left) The distance to the mirror is optimized to achieve the best resolution locally. (Right) The distance to the mirror is optimized to achieve the optimal working range and resolution across the entire scanned area.

The validity of the simulations should be investigated further. Unfortunately, only a small number of measurements could be performed on the lipid bilayer sample. Even though the simulations are straightforward, they do seem accurate enough on a first glance. Experimental measurements also contain instrumental disturbances. It speaks to the quality of the bilayer sample and instrumentation when a simple single exponential approximation can approach a similar result.

Chapter 6

Lateral Limitations of the LDOS Nano-ruler

In the previous chapter the axial resolution was thoroughly investigated. However, measurements on 2D surfaces also rely on the lateral resolving power. In this chapter we briefly examine several simulated surfaces and investigate whether the probe has any influence on the point spread function.

The LDOS nano-ruler is dependent on TCSPC data from a diffraction-limited area. Surface variations within this limited area will be reduced to a single distance. Even though the LDOS nano-ruler has an axial resolving power in the order of 10 nm, the lateral resolution is limited to roughly 300 nm (Fig. 6.1).

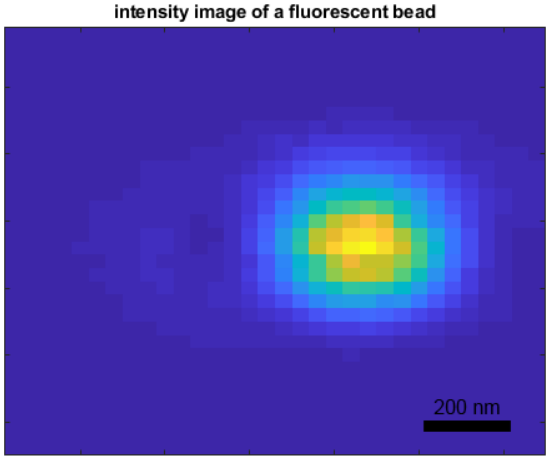

FIGURE 6.1: **Experimental determination of the point spread function.** The 40 nm fluorescent bead acts as a point-like radiating source. Scanning over a fluorescent bead with small increments reveals the point spread function of the device.

6.1 Simulations of Various Surface Scans

Current experiments are limited to flat surfaces and gratings. Furthermore, it has proven difficult to produce a single lipid bilayer that neatly covers a step surface (see Appendix B: "Covering Non-Flat Surfaces with a Lipid Bilayer"). To better understand the lateral limitations of the system, simulations were performed from simple steps to more complex surfaces.

To expand the simulations to surface scans, a MATLAB script was written to generate various surfaces. A single fluorophore point is generated every 10x10 nm. Every point has an x, y and z coordinate which allows for the surface to fold underneath itself. This is important for the simulation of membrane folds such as in caveolae.

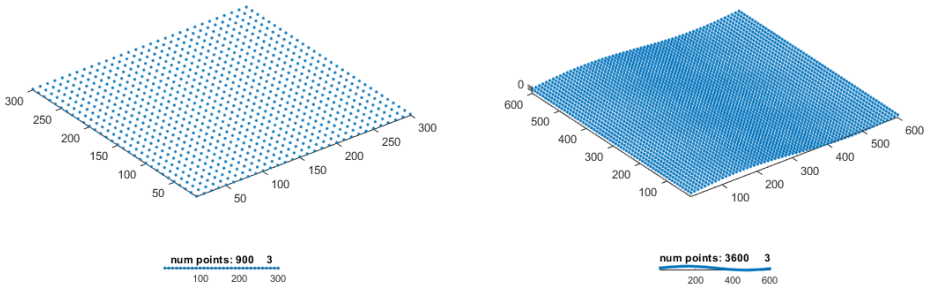

FIGURE 6.2: **Examples of generated surfaces.** (Left) A flat surface that is used as a base for surface generation. Typically a single measured area would be 300x300 nm. (Right) A larger sinusoidal surface is one of the variations that can be generated.

To determine the corresponding lifetime of a point, the mirror distance relative to 0 must be set. Variations within the surface will consequently lead to different mirror distances, and these distances are again translated into variations in lifetime using a smoothed $\tau(d)$ curve.

A measured area is typically set as 300x300 nm (the pixel size), this is also the point spread function of the system. The step size can vary but is also typically set as 300 nm.

Per simulated photon, the program will randomly select a point from the measured area. This point has a given lifetime and the arrival time of the photon is determined from a single exponential probability distribution, similarly to the simulations in Chapter 5.3: "Calculating the Axial Resolution Through Simulations". Per pixel, $20 \cdot 10^3$ photons were generated.

6.1.1 Surfaces Containing a Step

The step is one of the simplest features and acts as a stepping-off point towards more complex surfaces. We have some experience with the measurements on gratings, although we unfortunately do not have a lipid bilayer covered step for direct comparison. The distance to mirror was set at 185 nm.

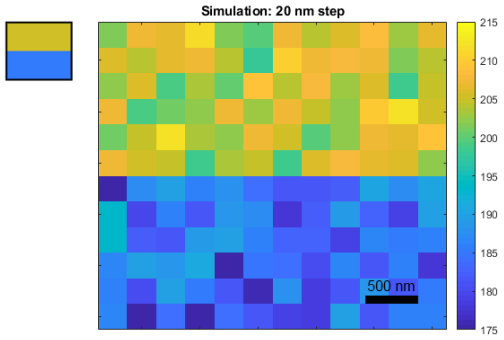

FIGURE 6.3: **A simulated measurement on a 20 nm step.** When the step is perfectly aligned with the scanning directions, the LDOS nano-ruler can neatly distinguish a 20n nm step. Distance to probe: 185 nm.

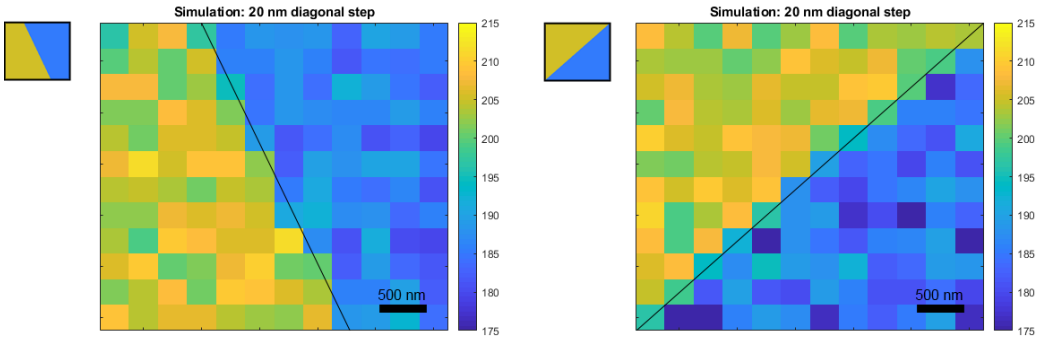

FIGURE 6.4: **Simulated measurements on 20 nm diagonal steps.** Changing the scan orientation with respect to the step has some influence on the measurements at the interface. (Right) A 45°angle returns an interface with a split contribution from both heights. Distance to probe: 185 nm.

The different angles of the steps represent a different scanning direction with respect to the step. Due to this change scan direction the interface becomes poorly defined. At the interface, a double exponential decay is registered, but it is fitted with a single exponential fit. When the amplitudes of the decays are equal (Fig. 6.4 (Right)), the single exponential fit does not return the average of the two lifetimes, but a lower than average lifetime.

6.1.2 Sinusoidal Surfaces

Since a step is not representative for the surface of a cell membrane, further simulations were run on sinusoidal surfaces. Multiple amplitudes and surface wavelengths were used to generate the various surfaces. The distance to mirror was set at 195 nm.

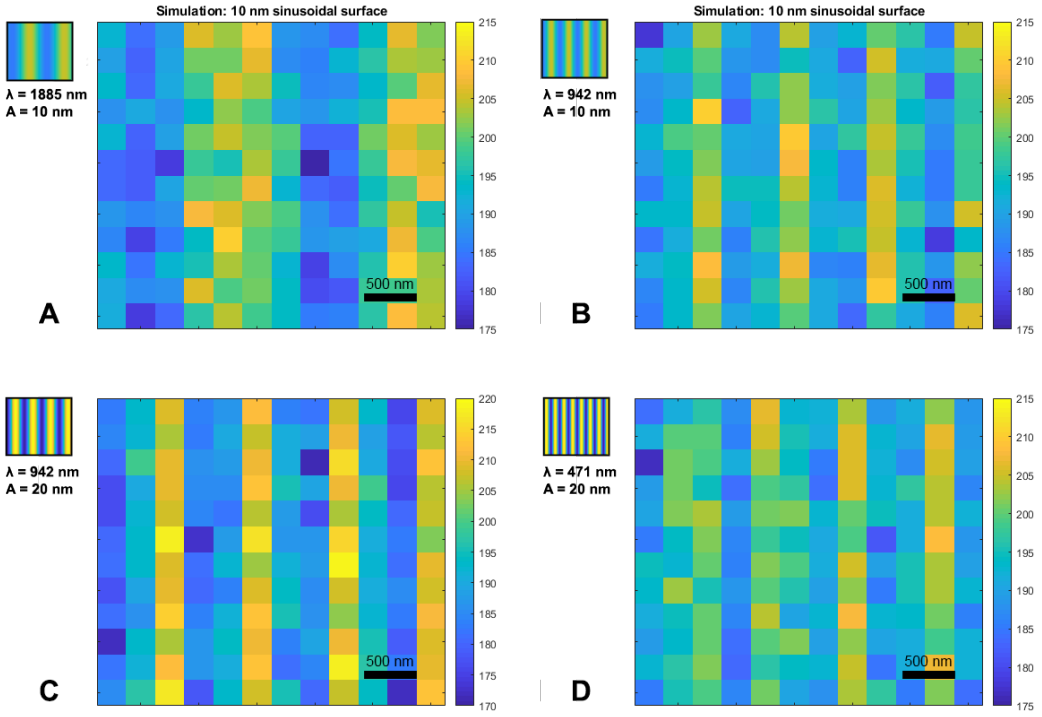

FIGURE 6.5: **Various simulated measurements on sinusoidal surfaces.** Different wavelengths and amplitudes were used to generate the surfaces. Wavelengths below the pixel size were not used: these cannot be distinguished via the current technique. Distance to probe: 195 nm. *Note that the bottom left image has a different color scale.*

The surface with the largest wavelength (or the lowest curvature), can still be properly resolved. When the wavelength however approaches the diffraction limit (< 1 μm), much of the information is lost as the original sine wave becomes more similar to a zigzag function (Fig 6.5C). As such, the surface from figure 6.5C ($A = 20nm$ and $\lambda = 942nm$) can still image the extrema (175 and 215 nm), however, when the the topography features become smaller (Fig 6.5D) this information is lost and the resulting image becomes flattened as a result. Topography features are caught within a pixel are averaged as a result. When these features approach the size of the pixel, the underlying surface can no longer be imaged.

6.1.3 Measuring a Nanoscale Feature: The Caveola

Previous studies regarding the LDOS nano-ruler have presented the need to study caveola-like structures in vivo. To investigate whether the LDOS nano-ruler has the capacity to resolve such features, a surface was generated with the assistance of a custom MATLAB script by Kabbani et al. [42]. In this paper membrane budding was simulated to reveal the effects of nanoscale curvature on single-molecule mobility. Such a membrane bud was redesigned to mimic a caveola on a flat surface (Fig. 6.6).

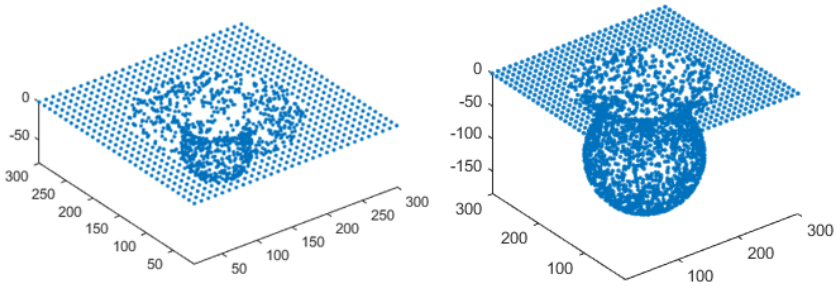

FIGURE 6.6: **A simulated caveola surface.** (Left) radius of curvature is 40 nm, a 20 nm radius connects the feature to the surrounding membrane and it extends up to 80 nm into the membrane. (Right) A far larger feature with a radius of 80 nm, a connecting radius of 40 nm and extending up to 185 nm into the membrane.

The simulations were then performed as before. However, the generated surface is smaller (1200 x 1200 nm) since we are dealing with such a small feature. The distance to mirror was also changed to 160 nm to accompany the large height differences within the surface.

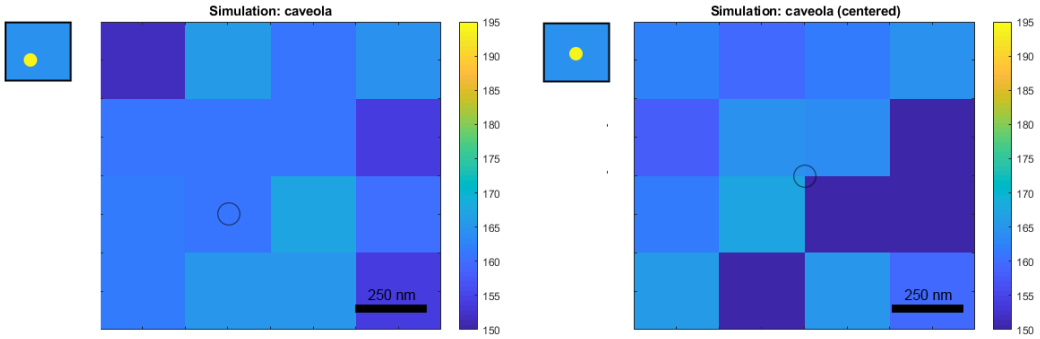

FIGURE 6.7: **Simulated measurements on flat surfaces with an caveola-like feature.** The small caveola feature ($r = 40nm$) is indistinguishable from the surrounding flat surface.

We can see that whether the feature is in a single pixel, or shared between multiple pixels, it is indistinguishable from the surrounding membrane. Resolving membrane features such as the caveola are the ultimate goal of membrane imaging, and the lateral resolution heavily limits the ability to resolve these features using the LDOS nano-ruler.

The larger caveola-like surface (Fig. 6.6 (Right)) was generated to still look at some effects of a sub-diffraction-limited feature.

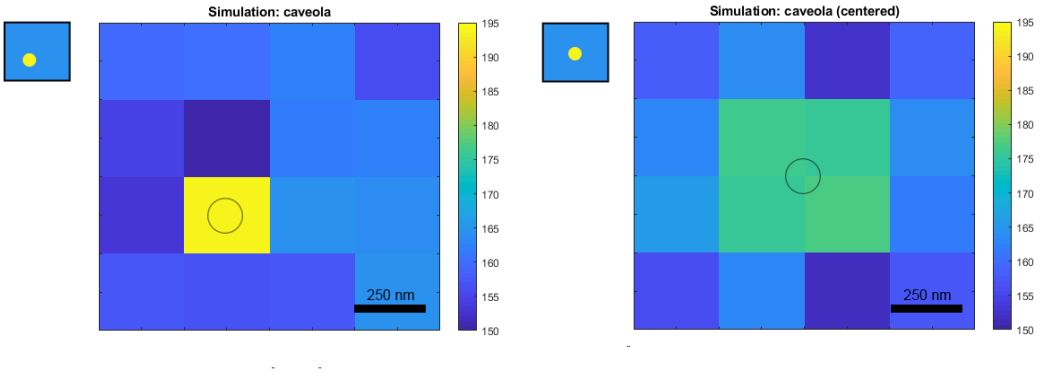

FIGURE 6.8: **Simulated measurements on flat surfaces with an large membrane undulation.** The location the scanned membrane feature is also crucial for the resulting image.

The location of the feature can be clearly seen in the scans. The difference between a single pixel scanning the feature, or multiple pixels scanning the feature is also evident. When the feature is shared within multiple pixels, the information is distributed over these pixels and the height information becomes muddled. Extreme undulations within the cell membrane can be detected but resolving an actual membrane topography in high detail seems beyond the capabilities of the LDOS nano-ruler.

6.2 Influence of the Probe on the Point Spread Function

Until now we have assumed that the point spread function (PSF) of the system remains fixed under proximity of the probe. To investigate this assumption, we have imaged several small fluorescent beads (FluoSpheres^{TM} NeutrAvidin^{TM}-Labeled Microspheres, 0.04 µm, red fluorescent (580/605), 1% solids). The beads were excited at a wavelength of 592 nm, with a 591/6 BP excitation filter and two 594 single-notch filters that act as the emission filter.

The beads were located with a large scan with the probe at 800 nm distance from the substrate. High resolution images were made to select a single bead. Subsequent scans were made with the probe lowering from 500 to 50 nm in 50 nm increments.

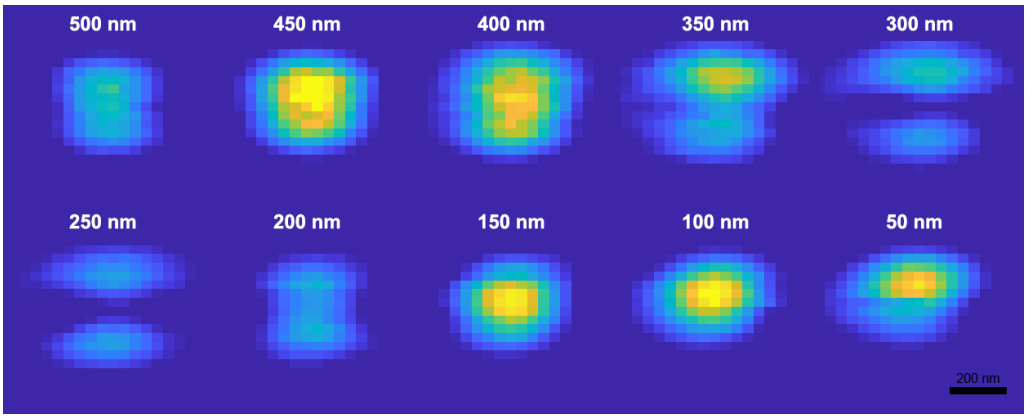

FIGURE 6.9: **The point spread function with the probe at decreasing mirror distances.** A fluorescent nanobead of 40 nm was scanned with 40 nm steps. The expected intensity dip is accompanied with the appearance of sidelobes. The intensity over all images is normalized.

Besides the intensity modulation, the PSF also changes in the presence of the probe. Between 450 and 150 nm, lobes appear that are unexpected. To further investigate the directionality of these lobes, the linear polarizer was rotated by 90°.

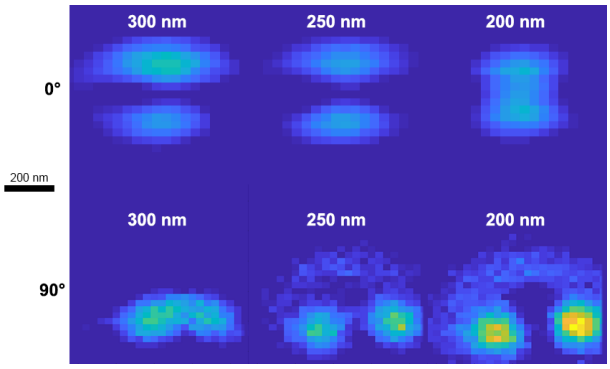

FIGURE 6.10: **Turning the linear polarizer changes the lobes in the PSF.**

It becomes obvious that when rotating the linear polarizer, the lobes of the PSF change accordingly. It is unclear what the cause is of the lobe formation.

6.3 Discussion

This chapter aimed to shed light on the lateral limitations of the LDOS nano-ruler. For this reason, simulations were used as an initial assessment. These simulations are an approximation, and even though the previous chapter showed that the lifetime distributions are comparable to that of a lipid bilayer, the generated surfaces and the scanning protocol was simplified in comparison to real measurements.

The generated surfaces were generated with a fluorophore point every 10x10 nm. This composition however is not representative of an average distribution over the surface, at steeper sections of the surface, less points are available in comparison to a flat section (Fig. 6.11). This causes flat surfaces to have a larger share in the generated photons.

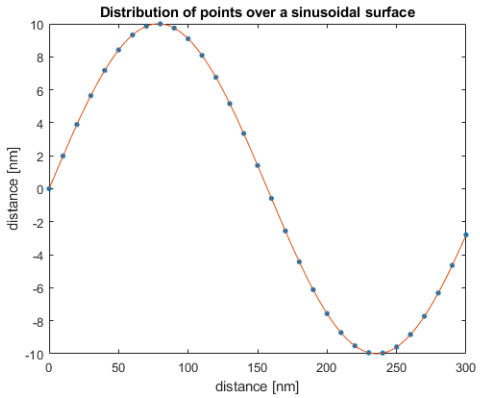

FIGURE 6.11: **The distribution of points across a sinusoidal line.** Points are randomly selected within a certain dimension, the density of points is larger around flat surfaces causing a bias towards this part of the surface.

The height variation of the large caveola-like feature (fig. 6.6 (Right)) extends up to 185 nm. This is far beyond the working range of the slope. The collected lifetimes therefor extend into the fourth region of the $\tau(d)$ curve. In chapter 7 we will attempt to overcome this limitation.

The point spread function used in scanning the surfaces is a two dimensional step function. In order to closer represent the LDOS nano-ruler measurement, a gaussian intensity distribution would be more accurate. Given more research into the PSF variation that was shown using the nanobeads, the varying PSFs could also be implemented to represent the measurement more accurately.

The distance-dependent changing of the PSF is initially an undesirable effect. Extreme differences in mirror distance within the diffraction-limited area could lead to an even more complicated effect. However, this effect could theoretically also be used to achieve a higher resolution, since the observed sidelobes are smaller than a diffraction-limited spot.

Chapter 7

Further Optimizations of the Technique

In chapter 5 we have seen that the LDOS nano-ruler can achieve a high axial resolution within a limited working range. In chapter 6 we observed that the lateral resolution severely limits our ability to image membrane curvatures of interest. In this chapter we propose some concepts to further expand the working range, and to improve the ability to scan more complex surfaces.

7.1 Expanding the Working Range with Two Point Measurements

The working range of the LDOS nano-ruler is limited to the regions between extrema. LDOS nano-ruler measurements on surfaces that extend beyond a single region encounter the issue that a single lifetime is not unique on the $\tau(d)$ curve and can correspond to multiple distances. In order to overcome this issue, the following method is proposed:

To differentiate between regions, measurements on the surface need to be uniquely defined on the $\tau(d)$ curve. To achieve this, a second lifetime measurement is performed with a different (known) mirror position compared to the initial lifetime measurement. Such a lifetime couple, the first and second lifetime measurement, is in fact unique across the entire $\tau(d)$ curve and grants us the ability to differentiate between regions. If we expand this technique across surface scans, this essentially means we will require two full lifetime surface scans to acquire a lifetime couple at each lateral position of the surface. The combination of the two acquired lifetimes, and the knowledge of the distance between these two lifetimes can single out exactly from which region the data is acquired.

To further illustrate this method, a stepwise approach is illustrated in figure 7.1. It shows the analysis of a generated staircase surface that spans 100 nm over region III and IV using the single lifetime method, and the analysis with the lifetime-couple method.

Figure 7.1A shows analysis of the surface using only region III to translate lifetimes into distances. Exclusively using this region is accompanied by two problems. Firstly, the staircase is not properly resolved. Instead of an showing an increasing staircase, the steps go up and then down again. Furthermore, when the measured

lifetime approaches an extrema on the $\tau(d)$ curve, the measured value can fall beyond this extreme due to the variation in lifetime. This lifetime then cannot be translated into a distance. This causes gaps within the analyzed surface.

The analyzed surface in figure 7.1C uses a second lifetime measurement at a predetermined distance from the first measurement. In this case, the second measurement has been performed with an increased mirror distance of 40 nm (e.g. the yellow and purple asterisk in 7.1B). Such a lifetime couple is unique across the $\tau(d)$ curve. The lifetime couple is subsequently used to scan across the $\tau(d)$ curve and the obtained lifetime differences (d_1 and d_2) between the couple and the $\tau(d)$ curve are squared (Fig. 7.1D).

$$\textit{Sum of squared lifetime difference} = d_1^2 + d_2^2$$

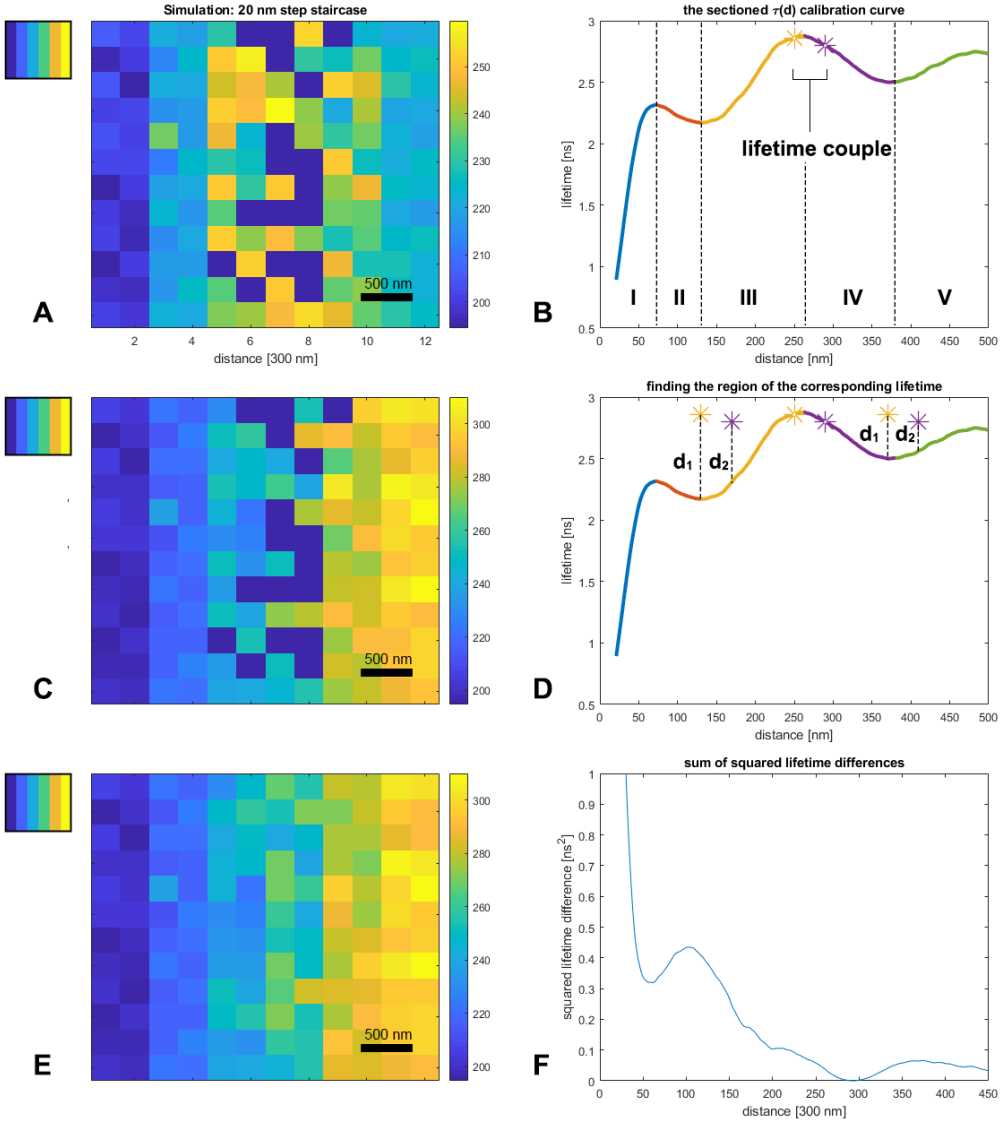

FIGURE 7.1: **Measuring a 20 nm step staircase over multiple region within the $\tau(d)$ curve.**

The resulting graph (Fig. 7.1F) has a minimum which correlates to the distance (location on the $\tau(d)$ curve) of the initial measurement. Here, the sum of squared

lifetime difference is at the lowest value, and at this distance the lifetime couple is located on top of the $\tau(d)$ curve. This then also identifies the region in which the measurements originate and we can select which region to use for the translation between lifetimes and distances. This routine is performed for every pixel on the measured surface.

Using this method, the staircase image follows the upward trend. However, since we are exclusively using the initial measurement for analysis, the problem around the extrema persists.

This problem can be resolved by using the second measurement not only as a region identifier, but also as useful data point. In order to choose the lifetime measurement with the highest possible resolution, the slope on the $\tau(d)$ curve is used to discriminate between the two lifetimes. Low slopes are abundant around extrema, and high slopes are found in the middle of the regions. A high slope corresponds with a higher resolution and are therefore preferred and used as selection criteria. Using this technique, the entire surface can be resolved (Fig. 7.1E). When both measurements are viable the one with the highest slope, and thus with the highest axial resolution, will be selected.

7.2 A Note on Lifetime Acquisition and Scanning Speed

The acquired TCSPC data must contain at least $5 \cdot 10^3$ collected photons in order to accurately determine the lifetime. Typically we collect at most 1 photon per 100 excitation pulses to prevent pile-up (see also section 2.1.2 Time Correlated Single Photon Counting). Furthermore, we must take into consideration that the emission intensity is also modulated with the distance to the mirror. Disregarding the first region (where the intensity approaches zero), $I_{max}/I_{min} \approx 10$ for the lipid bilayer with Rhodamine B. This is under the assumption that the fluorophore coverage is homogeneously distributed.

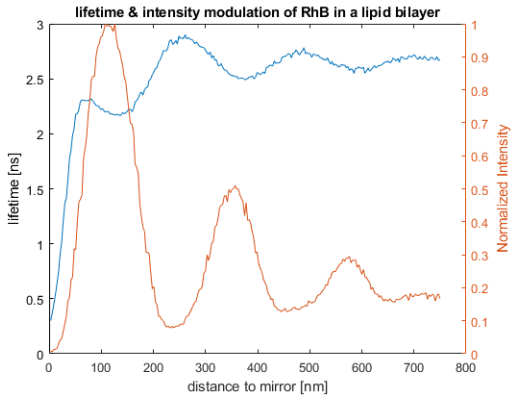

FIGURE 7.2: **The intensity modulation further influences the minimum dwell time.** At a constant laser power the number of collected photons fluctuates as the mirror approaches the surface. The laser power must be tuned to prevent photon pile-up. The dwell time at the intensity minimum therefore increases compared to the intensity maximum.

Taking all these factors into accounts, we can calculate the minimal dwell time needed to accurately determine a single lifetime.

$$minimum\ dwell\ time = \frac{\#\ of\ photons \times 100}{repetition\ rate\ [Hz]} \frac{I_{max}}{I_{min}} = \frac{5 \cdot 10^3 \times 100}{20 \cdot 10^6\ s^{-1}} \cdot 10 = 250\ ms$$

In addition to the acquisition time of the collected photons, the AFM cantilever is also given a certain time to relax between photon collection which increases the overall scanning time.

7.2.1 Improving Lifetime Acquisition

A straightforward way to reduce the dwell time is to increase the repetition rate. The intensity decay is typically measured for at least four times the mean decay time [29]. Increasing the repetition rate of the laser to 80 MHz would be feasible for Rhodamine B in the lipid bilayer since the peak lifetime is approximately 2.8 ns. This change would improve the dwell time by a factor of 4.

In figure 5.3 we have investigated the effect of the number of collected photons on the lifetime in a lipid bilayer. The dwell time could be further decreased by limiting the amount of collected photons. This will however increase the lifetime error as consequence, and therefore the uncertainty in the calculated distance.

The intensity modulation is large limiting factor, this can however also be reduced by limiting the working range. The second largest peak intensity is almost two times lower than the overall peak intensity. Avoiding the initial region could therefore reduce the I_{max}/I_{min} ratio and further reduce the dwell time.

7.3 Surpassing the Lateral Limitations

The lateral resolution of the LDOS nano-ruler is a limiting factor when resolving complex surfaces. In this section, we will quickly discuss possible methods to overcome this issue.

7.3.1 The LDOS Nano-Ruler and Super-Resolution Techniques

In section 1.2.1 "Optical Super-Resolution", several optical super-resolution techniques such as the STED and STORM are discussed that can beat the diffraction limit. Integrating these techniques could theoretically improve the lateral resolving power the LDOS nano-ruler lacks.

For lifetime measurements the photons have to be carefully collected, at most 1 photon per 100 excitation pulses. Combining lifetime measurements with STED would therefore require an immense amount of laser power to constantly deplete the surrounding region, making it unsuited for lifetime measurements.

The stochastical methods are difficult to combine with the LDOS nano-ruler. It further limits the use of the fluorophores since they need to be photoswitchable. The detector has to be able to detect arriving photons in a plane, as well as measure the arrival time. Lastly, the lifetime of the fluorophore is dependent on their orientation. For the LDOS nano-ruler, lifetime measurement cannot be reduced to single-molecules, and TCSPC data from multiple fluorophores would have to be combined.

It thus remains a large challenge to increase the lateral resolving power of the LDOS nano-ruler. However, without such an improvement, the technique will remain limited to measuring global curvatures.

7.3.2 Improved Lateral Resolution: What Could We See?

In order to get an idea for the imaging capabilities of a high resolution LDOS nanoruler, a simulation has been performed on the caveola surface we could not visualize in chapter 6 (Fig. 6.6). In this simulation, the step size and measuring area have been decreased to 100 nm and 100x100nm respectively.

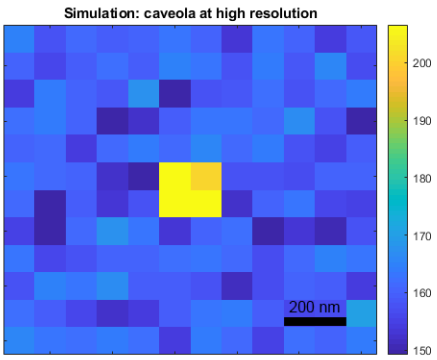

FIGURE 7.3: **The caveola can be located with a higher resolution of 100 nm.**

We can see that with the increased lateral resolution, we can locate the caveola. The caveola is still shared between the measured pixels. The actual caveola feature reaches a depth of 80 nm compared to the surrounding membrane (Fig. 6.6). This depth is still not resolved due to the curvature that occurs within the diffraction-limited area. But the contrast is high enough for localization.

7.4 Discussion

Expanding the working range is important to scan larger surfaces with large membrane undulations. The two-point approach expands the working range beyond multiple regions. The downside of this method is that the measurement time increases twofold. Another problem is that measuring the total surface twice could lead to discrepancies over time depending on the scan size. In this situation it is advised to measure the lifetime couple per pixel, which complicates the scanning procedure since the probe has to be dropped and raised per measured instance. This however makes sure that changes in the membrane over time are caught in a small timespan.

The distance between the lifetime couple could also be further optimized, 40 nm was chosen to bridge the gap over the extrema. But a larger distance gap between the lifetimes could lead to an improved resolution.

It has been previously suggested to use the intensity as a second indicator to differentiate between regions. Although this is possible it encounters two problems. Firstly, it will still not solve the issue that occurs near the peaks of the $\tau(d)$ curve, where recorded lifetimes can fall outside the calibrated extrema. Furthermore, membrane curvature and an inhomogeneous distribution of fluorophores lead to inconsistencies in perceived intensity, making it a more dubious method.

Chapter 8

Conclusion

In this project we have determined the axial resolution of the LDOS nano-ruler on multiple surfaces, identified some limitations of the device and suggested some improvements for future development.

First, we have identified that a polystyrene sample is unsuited for topography measurements. Variations in layer thickness that occur when spin-coating a surface lead to changes in the lifetime read-out, making it impossible to accurately determine distances. A lipid bilayer however has shown to be a good alternative with regards to lifetime measurements, showing close to no additional interaction with the AFM cantilever. The coverage of a non-flat surface with a lipid bilayer remains difficult, as these require more laborious techniques which require more tuning to work.

Second, the axial resolution of the LDOS nano-ruler has been determined. The axial resolution is dependent on the distance to the mirror, the collected photons, and the type of surface coverage. On polystyrene, the axial resolution varies from 9 to 28 nm at $20 \cdot 10^3$ collected photons. The lipid bilayer displayed even higher resolutions, ranging from 4 to 10 nm at $10 \cdot 10^3$ collected photons. The development of the axial resolution on a lipid bilayer has been investigated further using simulations. Gaps between regions where measurements are impossible were identified which allowed for accurate determination of the working range.

Third, the simulations were expanded to test which surface topography could be resolved by the LDOS nano-ruler. Membrane features which vary over roughly three times the diffraction-limited area ($\approx 1\mu m$) could still be properly resolved. Features much smaller than the diffraction-limit can't be resolved, or even located by the LDOS nano-ruler. Furthermore, measuring the point spread function on fluorescent nano-beads under influence of the probe revealed that the point spread function is heavely influenced by the probe. This phenomenon is influenced by the polarization by the light and is poorly understood.

Fourth, optimizations to the technique have been proposed to improve the working range and the scan speed. Measuring two lifetimes at different distances at a single location allows to bridge regions and expand the working range. Parameters that influence the dwell time are identified, and suggestions to further minimize the dwell time are proposed by a factor of at least 8. Optical super-resolution techniques are briefly considered for improving the lateral resolution. This however proves to be a daunting task since lifetime measurements and a low lateral resolution are difficult to combine. A higher lateral resolution is however desperately needed to advance the technique towards practical use. It has been shown that an increased lateral resolution allows for the localization of diffraction-limited membrane undulations such as in caveolae.

In conclusion, the LDOS nano-ruler has a high axial resolution on a properly labeled surface. Further development of the LDOS nano-ruler towards cell measurements remains challenging. With proper homogeneous labeling, global cell membrane curvatures could be measured. Measuring more complex membrane folds however requires a higher lateral resolving power.

8.1 Recommendations

Currently, the approach of the probe to the surface is a semi-manual process where the probe has to be in contact with the surface in order to calibrate its distance to the mirror. By analyzing the lifetime during descent, a controlled calibration could be performed without the probe making contact with the surface. This would prevent a large source of wear on the probe.

Laser intensity is currently mainly controlled by a series of ND filters. It has been suggested that being able to tune the laser power would give finer control. This would also allow for the dwell time to be minimized further if required.

Some difficulties were encountered while measuring in an aqueous environment. The probe has little space to move in when contained within the holder, limiting the measurable area. While areas of interest could be present outside the measurable area, the holder would prohibit these measurements as the probe would collide with the holder. A slight increase in the sample dimensions would allow for more freedom during experiments.

Current measurements on live cells are difficult to perform since the probe has to be positioned above the cell surface with a high angle. There are established techniques that culture cells in microwells, sometimes even providing a single-cell confinement. Developing such an sample would would allow for a easier probe management, since the AFM tip is elevated in comparison with the cell.

To check whether measurements on cells are possible, the reproducibility of the $\tau(d)$ curve needs to be investigated. Staining a cell membrane in a homogeneous manner is far more challenging than using the fluorescently labeled lipids used in this project. Establishing a reproducible $\tau(d)$ curve on a stained cell membrane is therefore advised.

It should be noted that although the way forward for measurements on cells is challenging, the current technique could already be suited for measuring distance variations such as in polymer brush swelling.

The influence of the LDOS on the PSF is poorly understood. Experiments with nanobeads should be repeated, and the effect of the polarization further investigated.

If the goals of the LDOS nano-ruler is to measure more complex membrane surfaces, the diffraction limit has to be overcome. Further research in the possibilities should be performed to conclude whether there is a practical way to enhance the lateral resolution.

Bibliography

[1] Nobutaka Hirokawa. Frontiers in Cell Biology: Articles, Kinesin and Dynein Superfamily Proteins and the Mechanism of Organelle Transport. *Science*, 279(January 1998):519–26, 1998. ISSN: 00368075. DOI: 10.1126/science.279.5350.519.

[2] B. Alberts. *Essential Cell Biology*. 3rd edition, 2010.

[3] Aditya Iyer and Mireille M.A.E. Claessens. Disruptive membrane interactions of alpha-synuclein aggregates. *Biochimica et Biophysica Acta - Proteins and Proteomics*, 1867(5):468–482, 2019. ISSN: 18781454. DOI: 10.1016/j.bbapap.2018.10.006. URL: https://doi.org/10.1016/j.bbapap.2018.10.006.

[4] Mary L. Kraft and Raehyun Kim. *Our evolving view of plasma membrane domains*. 2014. URL: https://www.asbmb.org/asbmbtoday/201409/LipidNews/.

[5] Gerrit Van Meer, Dennis R. Voelker, and Gerald W Feigenson. Membrane lipids: where they are. *Nature Reviews Molecular Cell Biology*, 101(1):1–4, 2009. ISSN: 1362-4962. DOI: 10.1038/nrm2330.Membrane. URL: http://pubs.acs.org/doi/abs/10.1021/ja401689b{\%}5Cnhttp://www.sciencemag.org/content/326/5959/1501.short{\%}5Cnhttp://www.pubmedcentral.nih.gov/articlerender.fcgi?artid=3497815{\&}tool=pmcentrez{\&}rendertype=abstract{\%}5Cnhttp://www.pubmedcentral.nih.gov/articlerende.

[6] Jean Rossier and Vincent Studer. *Nanoscience: Nanobiotechnology and Nanobiology*. 2010. ISBN: 9783642105586. DOI: 10.1007/978-3-540-88633-4.

[7] John Heuser. Three-Dimensional Visualization of Coated Vesicle Formation in Fibroblasts. 84(March):31–34, 1980.

[8] Anne J Ridley. Review Life at the Leading Edge. *Cell*, 145(7):1012–1022, 2011. ISSN: 0092-8674. DOI: 10.1016/j.cell.2011.06.010. URL: http://dx.doi.org/10.1016/j.cell.2011.06.010.

[9] Nicholas Ariotti, James Rae, Natalya Leneva, Charles Ferguson, Dorothy Loo, Satomi Okano, Michelle M. Hill, Piers Walser, Brett M. Collins, and Robert G. Parton. Molecular characterization of caveolin-induced membrane curvature. *Journal of Biological Chemistry*, 290(41):24875–24890, 2015. ISSN: 1083351X. DOI: 10.1074/jbc.M115.644336.

[10] Nicholas Ariotti, Manuel A. Fernández-Rojo, Yong Zhou, Michelle M. Hill, Travis L. Rodkey, Kerry L. Inder, Lukas B. Tanner, Markus R. Wenk, John F. Hancock, and Robert G. Parton. Caveolae regulate the nanoscale organization of the plasma membrane to remotely control Ras signaling. *Journal of Cell Biology*, 204(5):777–792, 2014. ISSN: 15408140. DOI: 10.1083/jcb.201307055.

[11] Bidisha Sinha, Darius Köster, Richard Ruez, Pauline Gonnord, Michele Bastiani, Daniel Abankwa, Radu V. Stan, Gillian Butler-Browne, Benoit Vedie, Ludger Johannes, Nobuhiro Morone, Robert G. Parton, Graa Raposo, Pierre Sens, Christophe Lamaze, and Pierre Nassoy. Cells respond to mechanical

stress by rapid disassembly of caveolae. *Cell*, 144(3):402–413, 2011. ISSN: 00928674. DOI: 10.1016/j.cell.2010.12.031.

[12] University of Cambridge Daniela A. Sahlender. *Clathrin-coated pit, inner leaflet of the plasma membrane*. URL: https://www.europeana.eu/portal/nl/record/9200579/mz82ne7p.html.

[13] Katherine Kalil, Li Li, and B. Ian Hutchins. Signaling mechanisms in cortical axon growth, guidance, and branching. *Frontiers in Neuroanatomy*, 5(SEP):1–15, 2011. ISSN: 16625129. DOI: 10.3389/fnana.2011.00062.

[14] Othon L. Gervásio, William D. Phillips, Louise Cole, and David G. Allen. Caveolae respond to cell stretch and contribute to stretch-induced signaling. *Journal of Cell Science*, 124(21):3581–3590, 2011. ISSN: 00219533. DOI: 10.1242/jcs.084376.

[15] Ingela Parmryd and Björn Önfelt. Consequences of membrane topography. *FEBS Journal*, 280(12):2775–2784, 2013. ISSN: 1742464X. DOI: 10.1111/febs.12209.

[16] Tomasz S Tkaczyk. *Tomasz S. Tkaczyk*. ISBN: 9780819472465.

[17] Stefan Hell W.; Far-Field Optical Nanoscopy. *Science*, 316(May):1153–1158, 2007.

[18] Bo Huang, Hazen Babcock, and Xiaowei Zhuang. Breaking the diffraction barrier: Super-resolution imaging of cells. *Cell*, 143(7):1047–1058, 2010. ISSN: 00928674. DOI: 10.1016/j.cell.2010.12.002. URL: http://dx.doi.org/10.1016/j.cell.2010.12.002.

[19] Lu Gan and Grant J. Jensen. Electron tomography of cells. *Quarterly Reviews of Biophysics*, 45(1):27–56, 2012. ISSN: 00335835. DOI: 10.1017/S0033583511000102.

[20] Yuekan Jiao and Tilman E. Schäffer. Accurate height and volume measurements on soft samples with the atomic force microscope. *Langmuir*, 20(23):10038–10045, 2004. ISSN: 07437463. DOI: 10.1021/la048650u.

[21] Patrick Happel and Irmgard D. Dietzel. Backstep scanning ion conductance microscopy as a tool for long term investigation of single living cells. *Journal of Nanobiotechnology*, 7:7, 2009. ISSN: 14773155. DOI: 10.1186/1477-3155-7-7.

[22] *Scientific Image - Atomic Force Microscope Illustration*. URL: https://www.nisenet.org/catalog/scientific-image-atomic-force-microscope-illustration.

[23] Yuri E. Korchev, Meera Raval, Max J. Lab, Julia Gorelik, Christopher R.W. Edwards, Trevor Rayment, and David Klenerman. Hybrid scanning ion conductance and scanning near-field optical microscopy for the study of living cells. *Biophysical Journal*, 78(5):2675–2679, 2000. ISSN: 00063495. DOI: 10.1016/S0006-3495(00)76811-1. URL: http://dx.doi.org/10.1016/S0006-3495(00)76811-1.

[24] Alexey I. Chizhik, Jan Rother, Ingo Gregor, Andreas Janshoff, and Jörg Enderlein. Metal-induced energy transfer for live cell nanoscopy. *Nature Photonics*, 8(2):124–127, 2014. ISSN: 17494885. DOI: 10.1038/nphoton.2013.345.

[25] Yanina Cesa, Christian Blum, Johanna M Van Den Broek, Allard P Mosk, Willem L Vos, and Vinod Subramaniam. Manipulation of the local density of photonic states to elucidate fluorescent protein emission rates:2525–2531, 2009. DOI: 10.1039/b817902f.

[26] R. Molenaar, J. C. Prangsma, K. O. Van Der Werf, M. L. Bennink, C. Blum, and V. Subramaniam. Microcantilever based distance control between a probe and a surface. *Review of Scientific Instruments*, 86(6), 2015. ISSN: 10897623. DOI: 10.1063/1.4922885. arXiv: 1502.03305.

[27] V. Subramaniam W.L. Vos C. Blum J.C. Prangsma R. Molenaar. Dark fraction in red fluorescent proteins determined by quantitative nanophotonic manipulation explains low overall quantum efficiency. *Manuscript*.

[28] N. Mateos, R. Molenaar, M. M. A. E. Claessens, and C. Blum. Photonic emitter manipulation to sample nanoscale topography. *Optics Express*, 27(8):11698, 2019. ISSN: 1094-4087. DOI: 10.1364/OE.27.011698. URL: https://www.osapublishing.org/abstract.cfm?URI=oe-27-8-11698.

[29] Joseph R. Lakowicz. *Principles of Fluorescence Spectroscopy*, number 5. 2006. ISBN: 9780387312781.

[30] ThermoFisher Scientific. *Fluorescence SpectraViewer*. URL: https://www.thermofisher.com/nl/en/home/life-science/cell-analysis/labeling-chemistry/fluorescence-spectraviewer.html.

[31] W. L. Barnes. Fluorescence near interfaces: The role of photonic mode density. *Journal of Modern Optics*, 45(4):661–699, 1998. ISSN: 13623044. DOI: 10.1080/09500349808230614.

[32] K. H. Drexhage. Influence of a dielectric interface on fluorescence decay time. *Journal of Luminescence*, 1-2(C):693–701, 1970. ISSN: 00222313. DOI: 10.1016/0022-2313(70)90082-7.

[33] R. R. Chance, A. H. Miller, A. Prock, and R. Silbey. Fluorescence and energy transfer near interfaces: The complete and quantitative description of the Eu+3/mirror systems. *The Journal of Chemical Physics*, 63(4):1589–1595, 1975. ISSN: 00219606. DOI: 10.1063/1.431483.

[34] R. R. Chance, A. H. Miller, A. Prock, and R. Silbey. Fluorescence and energy transfer near interfaces: The complete and quantitative description of the Eu+3/mirror systems. *The Journal of Chemical Physics*, 63(4):1589–1595, 1975. ISSN: 00219606. DOI: 10.1063/1.431483.

[35] R. Amos and W. Barnes. Modification of the spontaneous emission rate of ions close to a thin metal mirror. *Physical Review B - Condensed Matter and Materials Physics*, 55(11):7249–7254, 1997. ISSN: 1550235X. DOI: 10.1103/PhysRevB.55.7249.

[36] N. Mateos. Photonic emitter manipulation to achieve axial super-resolution for in vivo cell membrane topography studies. *Manuscript*.

[37] *Interchangeable Coverglass Dish - Bioptechs*. c2019, [accessed 2020, August 31]. URL: https://bioptechs.com/product/interchangeable-coverglass-dish/.

[38] Ralf P. Richter, Rémi Bérat, and Alain R. Brisson. Formation of solid-supported lipid bilayers: An integrated view. *Langmuir*, 22(8):3497–3505, 2006. ISSN: 07437463. DOI: 10.1021/la052687c.

[39] G.T Barnes and I.R Gentle. *Interfacial science: an introduction*. Oxford University Press, New York, 2nd editio edition, 2011, page 326. ISBN: 978-0-19957118-5.

[40] Molly C. Larsen. Binary phase diagrams at the air-water interface: An experiment for undergraduate physical chemistry students. *Journal of Chemical Education*, 91(4):597–601, 2014. ISSN: 19381328. DOI: 10.1021/ed4004854.

[41] David E. Wolf. *The optics of microscope image formation*, volume 114. Elsevier Inc., 4th edition, 2013, pages 11–42. ISBN: 9780124077614. DOI: 10.1016/B978-0-12-407761-4.00002-6. URL: http://dx.doi.org/10.1016/B978-0-12-407761-4.00002-6.

[42] Abir Maarouf Kabbani, Xinxin Woodward, and Christopher V. Kelly. Revealing the effects of nanoscale membrane curvature on lipid mobility. *Membranes*, 7(4), 2017. ISSN: 20770375. DOI: 10.3390/membranes7040060. arXiv: 1706.00087.

Appendix A

AFM-PS Interaction

Early experiments were mainly performed on a polystyrene covered surfaces. We quickly observed that there was interaction between the AFM tip and the polystyrene. This was first observed in lifetime measurements, where a clear line artifact was observed (Fig. A.1).

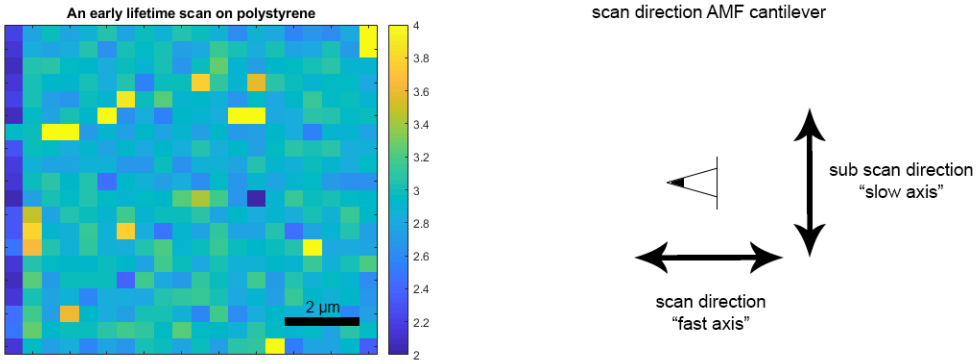

FIGURE A.1: **Early lifetime measurements showed a clear artifact.** (Left) An early lifetime scan of a flat polystyrene layer. The artifact became more apparent in region I, where slight variations in distance-to-mirror are accompanied by large lifetime deviations. (Right) The scanning direction of the cantilever.

We investigated this interaction further on an AFM system. Since the probe is allowed to be lowered at least 1200 nm on contact, a comparable force was recreated on a different cantilever. With $k_{LDOS} = 0.03N/m$ and $k_{AFM} = 0.06N/m$:

$$1500nm \cdot 0.03N/m = 45nN$$

$$d = \frac{45nN}{0.6N/m} = 75nm$$

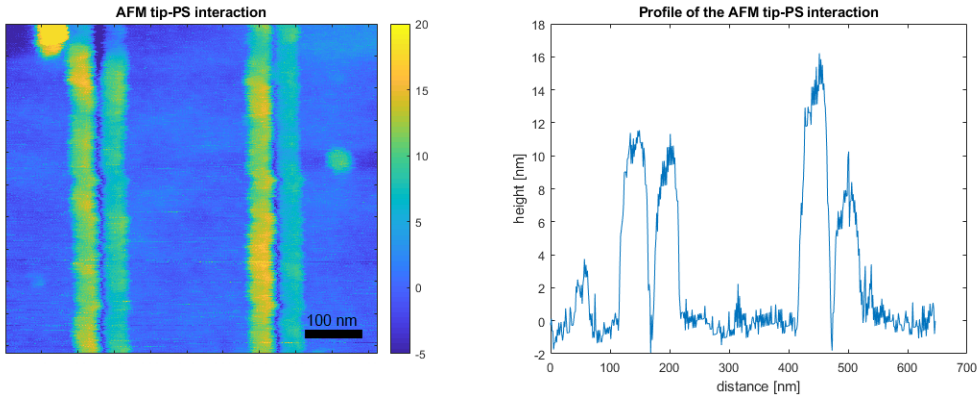

FIGURE A.2: **The interaction between an AFM tip and a polystyrene layer.** (Left) The AFM tip has "digged" two vertical lines with the polystrene at a comparable force to the LDOS cantilever. (Right) The profile of the polystyrene after the mimicked line scans.

Here it became evident that there was significant interaction between the AFM-tip and the polystyrene surface. We can conclude that this "digging" effect is the likely origin of the artifact (Fig. A.1). As the cantilever always scans in one direction - from left to right - it will continue to the next line after a horizontal retrace. This retrace occurs much faster, and most likely causes the discrepancy.

Appendix B

Covering Non-Flat Surfaces with a Lipid Bilayer

There have been several attempts to cover gratings with a lipid bilayer. The lipid bilayer should resemble a more physiological environment and reduce the AFM-PS interaction (Appendix A). Similar to a deposited polystyrene layer, the lipid bilayer should cover the glass coverslip homogeneously.

Initially we used the vesicle deposition method, which worked extremely well for flat surfaces. This however proved unsuccessful for the grating, as the deposition was not homogeneous in the end (Fig. B.1).

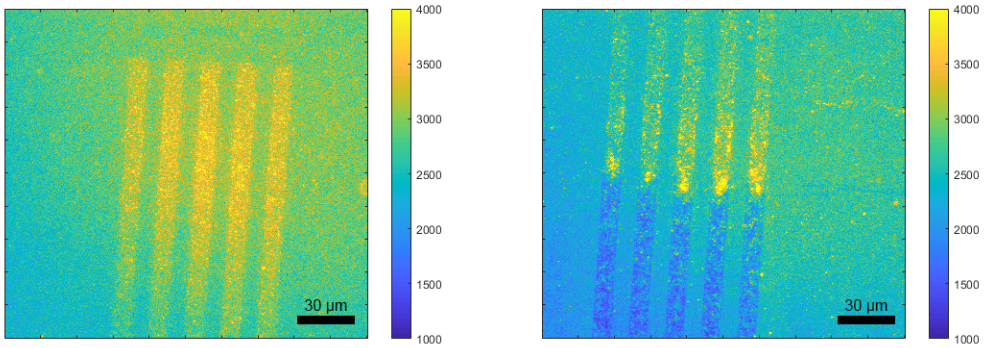

FIGURE B.1: **Gratings covered with lipids using vesicle deposition.** The gratings tended to fill up with multiple bilayers, or not fill up at all. Even if a small section was properly covered, it is nearly impossible find this section again under the LDOS set-up.

The gratings tended to fill up with multiple lipid layers. Even though small sections seemed to be covered properly, it was nearly impossible to retrace the region under the LDOS set-up.

Since vesicle deposition would not cover the grating in a sufficient manner, other deposition methods were attempted. Initially dipcoating was performed to overcome the coverage issue. Although this led to better coverage, the fluorophores bleached must faster compared to the vesicle deposited sample. This difference could however also originate from the different treatments to make the surface hydrophilic. For dipcoating, a NaOH treatment was typically used. It is possible that a lack of washing steps could have affected the surface layer.

Langmuir-Blodgett (LB) Deposition was finally used to cover the gratings. Unfortunately, during deposition the surface pressure never reached plateau (indicating the required liquid-condensed phase, see section 3.3.2 "Langmuir-Blodgett Deposition"). In theory, this technique should ensure a homogeneous coverage. It is therefor recommended that Langmuir-Blodgett deposition is further investigated for the fabrication of future samples. Samples that were prepared using LB deposition during this study were unsuited for LDOS measurements.

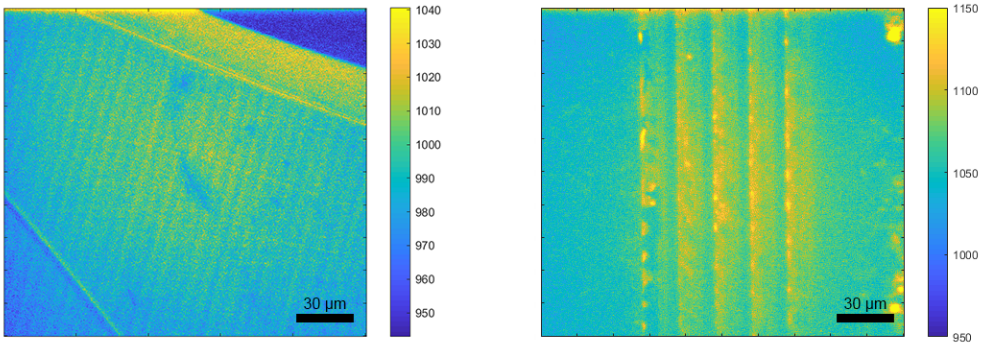

FIGURE B.2: **Lipid bilayer coverage using dipcoating methods.** (Left) Dipcoating led to decent coverage, but with a sinusoidal pattern. (Right) Langmuir-Blodgett Deposition was attempted on multiple samples, however the monolayer film never reached the required liquid-condensed phase for proper deposition.

B.1 Protocol: Vesicle Deposition

B.1.1 Materials

Lipid solution (200 µL DOPC (10 mg/mL), 20 µL DOPE-Rh (1 mg/mL), 1 mL Chloroform)
0.2 µm pore filter (cellulose acetate)
PBS (1x)
Cleaned coverslip

B.1.2 Procedure

1. Dry the lipid solution under a gentle N_2 gas stream for 15 minutes under a fume hood.
2. Resuspend the lipid cake in 1.2 mL MilliQ
3. Vortex the solution to promote the formation of liposomes
4. Filter the vortexed solution through a 0.2 µm pore wetted filter 10x.
5. The vesicle mix can be stored up to two weeks at 4 °C
6. Create the SLB solution by mixing the vesicle solution, PBS (1x) and MilliQ (2:1:1), approximately 300 µL is sufficient for a glass coverslip
7. Deposit the SLB solution on a hydrophilic substrate (UV treatment), and incubate for 120 minutes
8. Wash the sample with a 1 mL pipette approximately 5 times, removing unwanted lipid deposition.

B.2 Protocol: Dipcoating

B.2.1 Materials

Lipid solution (20 µL DOPC (10 mg/mL), 2 µL DOPE-Rh (1 mg/mL), 0.5 mL Chloroform)
PBS (1x)
Cleaned beaker (Mucasol > MilliQ > Ethanol/Aceton/Isapropanol/MilliQ mixture, ultrasonic baths for 10 min.)
Cleaned coverslip
Blower balloon
Dip coating set-up (ME-111 in the flow box)

The controller
Speed down: 0.5
Speed up: 0.5
Travel dist.: 45 mm (standard value)
Pause: 0.24 (24 sec) (standard value)
To operate: first press reset, then start.

B.2.2 Procedure

1. Run a test with the controller to adjust speed and height
   - Press reset
   - Put the substrate in the clamp
   - When totally to the bottom (lamp is blinking): press stop
2. Clean the substrate and hang them in the clamp in the dipcoat device
3. Immerse them directly in the beaker filled with PBS (1x)
4. Add 0.5 mL of lipid solution, enough to cover the whole surface
5. Let stand for 30 min to form planar interfacial layer
6. Raise the substrate slowly with controlled rate (with help of controller), letting the lipid layer deposit at the substrate. After a short pause, the controller will lower itself for the deposition of the second layer.
7. Raise the substrate, lock it in the holder and cover them with sufficient PBS (1x) for transport.

B.3 Protocol: Langmuir-Blodgett Deposition

B.3.1 Materials

Dedicate glassware, spoons and chemical stocks only for LB work
Special spoon for LB only (at cupboard Ellipsometer lab)
Glassware 2 L flask, big 2L bottle, beaker (50mL) and the small flasks (10ml) for LB only
Soap 1:1 molar ratio of Octanoic acid/KOH (at sink chem lab)
Lipid solution (20 µL DOPC (10 mg/mL), 2 µL DOPE-Rh (1 mg/mL), 0.5 mL Chloroform)
Chloroform 99,8% pure (sigma-aldrich, #288306, safety cupboard 104G) Mw=284.48
PBS (1x)
Glass syringe and needle
Software Nima TR 7.8
Langmuir-Blodgett trough
Dust free tissue

B.3.2 Safety

Chloroform - Use gloves, googles and fume hood/ventilation arm

Recipe for the special soap:
The soap is prepared with Octanoic acid (liquid) and KOH (power), with the molar ratio of 1:1. See below for the LB soap recipe

Molar	chemical	mL	Mw	mol	g
1	KOH		56,1	0,05	2,805
1	octanoic acid		144,2	0,05	7,21
	water (ml)	42,08			

TABLE B.1: **Soap recipe (20190123) for 50 mL. Molar ratio 1:1 KOH and octanoic acid.**

B.3.3 Procedure

EVERY TIME BEFORE MEASUREMENT

- Thoroughly cleaning of glass ware to be used with octanoic acid-KOH soap
- Calibration of LB through
- Thoroughly cleaning of LB trough with water/ethanol/Chloroform
- Preparation of subphase and monolayer > create pressure isotherm graph
- Deposition of monolayer onto substrate

1. Prior to every experiment clean all the glass ware: the 2 L flask, big 2L bottle, beaker (50mL) and the small flasks (10ml). First clean everything with special LB soap, and then with plenty of DI water until you cannot smell any soap from the glassware.
2. Prepare lipid solution (20 µL DOPC (10 mg/mL), 2 µL DOPE-Rh (1 mg/mL), 0.5 mL Chloroform).
3. Prepare subphase; 2 L PBS (1x) buffer solution.
4. Prepare the substrates by cleaning them in a beaker with isopropanol and ethanol and put 15' in sonication bath. Flush with EtOH. Put in plasma cleaner or UV-ozone cleaner for 20'.
5. Clean the LB trough thoroughly and the walls of the box around the LB trough to get rid of dust particles. Fill whole tray with DI water, remove, wipe with tissue soaked in ethanol and thereafter tissue soaked in Chloroform. Fill once again the whole tray with DI water and remove.
6. Switch on the computer and the Nima-box transferrer (password: ew1002m/b). Perform calibration of the pressure detector. Enable calibrations in the menu setup > calibration > enable > pressure. Measure the empty weight pan. Measure the pan+weight and note the calibration factor ($\sim$0.0046).
7. Then pour $\sim$1L sub phase solution into the trough. Clean the barriers and put them with the holders on the surface. Clean the solution surface with the vacuum pump.
8. Hang a Wilhelmi plate on 3/4 hooks so it is wetted by the subphase. Lift the plate above surface manually (knob at back of hook). Make Pi = zero and lower the Wilhelmi plate 2mm in the subphase. Pi should be 70.0 mM/m (+/- 6mN/m). Re-zero Pi.

9. Check the surface tension by compressing the barriers till closing area. Pi should be $\sim$ 0.1 mN/m at end of pressure isotherm, which suggests surface clean enough. The cleaning needs to be done several times to let the surface tension drop to 0.1mN/m ($\sim$3X). Put the substrates inside the solution, check the surface tension again. If surface tension is not good, or when it peaks a bit before closing area (e.g. 40cm^2), then clean the surface again. Delete all runs.
10. Spread 150 µL lipid solution onto the solution surface with the Hamilton micro syringe. Put it drop wise on surface in an equal way, $\sim$15 drops in total. Close the box around the LB trough to avoid dust on the surface. Leave it there for 30 min to make sure the chloroform evaporates and lipid molecules spread evenly on the surface.
11. Check all the parameters in the software. Start to compress the barriers, it will stop till a certain pressure (>40mN/m). Then raise and lower the substrates (set pressure control in menu).
12. Remove the upper layer of the rest solution in the trough (with the pump sucking the solution out), removing the remaining lipids.
13. Remove the substrates from the solution.
14. Clean the trough with plenty of chloroform and DI water again.
15. Clean all the glass wares and fill them with DI water, and seal them again with parafilm.

Preferences Nima software
Monolayer menu
Open to area = 500 cm^2
Close to area = 40 cm^2
Mol. weight = 284.48 g/mol
Conc = 1 mg/mL
Volume dispense = 50 µL
Click: accept
Pi= -0.1 t/m 0.1 mN/m
Barrier menu
Speed = 10cm^2/min (> put on 100 or 500 cm^2/min when checking clearness surface)
Change *bar speed control* to *pressure control*
Set Pi = 0 pressure and speed = 10
Target = 30 mN/m, gain = 5

First layer up
Layer req =2
End stop= 75-15
Speed= 2 up to 2

Surface tension water H2O Pi = -68,9mN/m

Appendix C

Derivation of the Full Width Half Maximum of a Normal Distribution

The probability density function for a Gaussian distribution is

$$f(x) = \frac{1}{\sigma\sqrt{2\pi}} e^{-\frac{(x-\mu)^2}{2\sigma^2}}$$

If we consider the distribution centered around 0 ($\mu = 0$), the FWHM is the distance between $-x_w$ and $+x_w$, who are located at half of the height of the peak. We can find x_w that will produce $f(x_w) = f(\mu)/2$

$$f(x) = \frac{1}{\sigma\sqrt{2\pi}} e^{-\frac{x_w^2}{2\sigma^2}} = f(\mu)/2 = \frac{1}{2\sigma\sqrt{2\pi}}$$

For $\sigma \neq 0$ and solving for x_w:

$$\frac{1}{\sigma\sqrt{2\pi}} e^{-\frac{x_w^2}{2\sigma^2}} = \frac{1}{2\sigma\sqrt{2\pi}}$$

$$e^{-\frac{x_w^2}{2\sigma^2}} = \frac{1}{2}$$

$$\frac{x_w^2}{2\sigma^2} = ln(2)$$

$$x_w^2 = 2\sigma^2 ln(2)$$

$$x_w = \pm\sqrt{2\sigma^2 ln(2)}$$

$$x_w = \pm\sqrt{2ln(2)} \cdot \sigma$$

The FWHM is then the distance between the two x_w coordinates

$$FWHM = +x_w - (-x_w) = 2x_w$$

$$FWHM = 2\sqrt{2ln(2)} \cdot \sigma$$